EUROPEAN ORGANIZATION FOR NUCLEAR RESEARCH

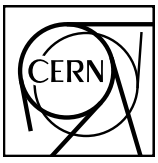

CERN-PH-EP-2012–350
November 26, 2012

Leading and Next-to-Leading Order Gluon Polarisation in the Nucleon and Longitudinal Double Spin Asymmetries from Open Charm Muoproduction

The COMPASS Collaboration

Abstract

The gluon polarisation in the nucleon was measured using open charm production by scattering 160 GeV/c polarised muons off longitudinally polarised protons or deuterons. The data were taken by the COMPASS collaboration between 2002 and 2007. A detailed account is given of the analysis method that includes the application of neural networks. Several decay channels of D^0 mesons are investigated. Longitudinal spin asymmetries of the D meson production cross-sections are extracted in bins of D^0 transverse momentum and energy. At leading order QCD accuracy the average gluon polarisation is determined as $\langle \Delta g/g \rangle^{\mathrm{LO}} = -0.06 \pm 0.21\ (\mathrm{stat.}) \pm 0.08\ (\mathrm{syst.})$ at the scale $\langle \mu^2 \rangle \approx 13\,(\mathrm{GeV}/c)^2$ and an average gluon momentum fraction $\langle x \rangle \approx 0.11$. For the first time, the average gluon polarisation is also obtained at next-to-leading order QCD accuracy as $\langle \Delta g/g \rangle^{\mathrm{NLO}} = -0.13 \pm 0.15\ (\mathrm{stat.}) \pm 0.15\ (\mathrm{syst.})$ at the scale $\langle \mu^2 \rangle \approx 13\,(\mathrm{GeV}/c)^2$ and $\langle x \rangle \approx 0.20$.

(to be submitted to The Physical Review D)

The COMPASS Collaboration

C. Adolph[8], M.G. Alekseev[24], V.Yu. Alexakhin[7], Yu. Alexandrov[15,*], G.D. Alexeev[7], A. Amoroso[27], A.A. Antonov[7], A. Austregesilo[10,17], B. Badełek[30], F. Balestra[27], J. Barth[4], G. Baum[1], Y. Bedfer[22], A. Berlin[2], J. Bernhard[13], R. Bertini[27], M. Bettinelli[16], K. Bicker[10,17], J. Bieling[4], R. Birsa[24], J. Bisplinghoff[3], P. Bordalo[12,a], F. Bradamante[25], C. Braun[8], A. Bravar[24], A. Bressan[25], M. Büchele[9], E. Burtin[22], L. Capozza[22], M. Chiosso[27], S.U. Chung[17], A. Cicuttin[26], M.L. Crespo[26], S. Dalla Torre[24], S. Das[6], S.S. Dasgupta[6], S. Dasgupta[6], O.Yu. Denisov[28], L. Dhara[6], S.V. Donskov[21], N. Doshita[32], V. Duic[25], W. Dünnweber[16], M. Dziewiecki[31], A. Efremov[7], C. Elia[25], P.D. Eversheim[3], W. Eyrich[8], M. Faessler[16], A. Ferrero[22], A. Filin[21], M. Finger[19], M. Finger jr.[7], H. Fischer[9], C. Franco[12], N. du Fresne von Hohenesche[13,10], J.M. Friedrich[17], V. Frolov[10], R. Garfagnini[27], F. Gautheron[2], O.P. Gavrichtchouk[7], S. Gerassimov[15,17], R. Geyer[16], M. Giorgi[25], I. Gnesi[27], B. Gobbo[24], S. Goertz[4], S. Grabmüller[17], A. Grasso[27], B. Grube[17], R. Gushterski[7], A. Guskov[7], T. Guthörl[9,b], F. Haas[17], D. von Harrach[13], F.H. Heinsius[9], F. Herrmann[9], C. Heß[2], F. Hinterberger[3], N. Horikawa[18,c], Ch. Höppner[17], N. d'Hose[22], S. Huber[17], S. Ishimoto[32,d], O. Ivanov[7], Yu. Ivanshin[7], T. Iwata[32], R. Jahn[3], V. Jary[20], P. Jasinski[13], R. Joosten[3], E. Kabuß[13], D. Kang[13], B. Ketzer[17], G.V. Khaustov[21], Yu.A. Khokhlov[21], Yu. Kisselev[2], F. Klein[4], K. Klimaszewski[30], S. Koblitz[13], J.H. Koivuniemi[2], V.N. Kolosov[21], K. Kondo[32], K. Königsmann[9], I. Konorov[15,17], V.F. Konstantinov[21], A. Korzenev[22,e], A.M. Kotzinian[27], O. Kouznetsov[7,22], M. Krämer[17], Z.V. Kroumchtein[7], F. Kunne[22], K. Kurek[30], L. Lauser[9], A.A. Lednev[21], A. Lehmann[8], S. Levorato[25], J. Lichtenstadt[23], T. Liska[20], A. Maggiora[28], A. Magnon[22], N. Makke[22,25], G.K. Mallot[10], A. Mann[17], C. Marchand[22], A. Martin[25], J. Marzec[31], T. Matsuda[14], G. Meshcheryakov[7], W. Meyer[2], T. Michigami[32], Yu.V. Mikhailov[21], A. Morreale[22,f], A. Mutter[9,13], A. Nagaytsev[7], T. Nagel[17], F. Nerling[9], S. Neubert[17], D. Neyret[22], V.I. Nikolaenko[21], W.-D. Nowak[9], A.S. Nunes[12], A.G. Olshevsky[7], M. Ostrick[13], A. Padee[31], R. Panknin[4], D. Panzieri[29], B. Parsamyan[27], S. Paul[17], E. Perevalova[7], G. Pesaro[25], D.V. Peshekhonov[7], G. Piragino[27], S. Platchkov[22], J. Pochodzalla[13], J. Polak[11,25], V.A. Polyakov[21], J. Pretz[4,g], M. Quaresma[12], C. Quintans[12], J.-F. Rajotte[16], S. Ramos[12,a], V. Rapatsky[7], G. Reicherz[2], E. Rocco[10], E. Rondio[30], N.S. Rossiyskaya[7], D.I. Ryabchikov[21], V.D. Samoylenko[21], A. Sandacz[30], M.G. Sapozhnikov[7], S. Sarkar[6], I.A. Savin[7], G. Sbrizzai[25], P. Schiavon[25], C. Schill[9], T. Schlüter[16], A. Schmidt[8], K. Schmidt[9,b], L. Schmitt[17,h], H. Schmïden[3], K. Schönning[10], S. Schopferer[9], M. Schott[10], O.Yu. Shevchenko[7], L. Silva[12], L. Sinha[6], A.N. Sissakian[7,*], M. Slunecka[7], G.I. Smirnov[7], S. Sosio[27], F. Sozzi[24], A. Srnka[5], L. Steiger[24], M. Stolarski[12], M. Sulc[11], R. Sulej[30], H. Suzuki[32,c], P. Sznajder[30], S. Takekawa[28], J. Ter Wolbeek[9,b], S. Tessaro[24], F. Tessarotto[24], L.G. Tkatchev[7], S. Uhl[17], I. Uman[16], M. Vandenbroucke[22], M. Virius[20], N.V. Vlassov[7], L. Wang[2], T. Weisrock[13], M. Wilfert[13], R. Windmolders[4], W. Wiślicki[30], H. Wollny[22], K. Zaremba[31], M. Zavertyaev[15], E. Zemlyanichkina[7], M. Ziembicki[31], N. Zhuravlev[7] and A. Zvyagin[16]

[1] Universität Bielefeld, Fakultät für Physik, 33501 Bielefeld, Germany[i]
[2] Universität Bochum, Institut für Experimentalphysik, 44780 Bochum, Germany[i]
[3] Universität Bonn, Helmholtz-Institut für Strahlen- und Kernphysik, 53115 Bonn, Germany[i]
[4] Universität Bonn, Physikalisches Institut, 53115 Bonn, Germany[i]
[5] Institute of Scientific Instruments, AS CR, 61264 Brno, Czech Republic[j]
[6] Matrivani Institute of Experimental Research & Education, Calcutta-700 030, India[k]
[7] Joint Institute for Nuclear Research, 141980 Dubna, Moscow region, Russia[l]
[8] Universität Erlangen–Nürnberg, Physikalisches Institut, 91054 Erlangen, Germany[i]
[9] Universität Freiburg, Physikalisches Institut, 79104 Freiburg, Germany[i]
[10] CERN, 1211 Geneva 23, Switzerland
[11] Technical University in Liberec, 46117 Liberec, Czech Republic[j]
[12] LIP, 1000-149 Lisbon, Portugal[m]
[13] Universität Mainz, Institut für Kernphysik, 55099 Mainz, Germany[i]

[14] University of Miyazaki, Miyazaki 889-2192, Japan[n]
[15] Lebedev Physical Institute, 119991 Moscow, Russia
[16] Ludwig-Maximilians-Universität München, Department für Physik, 80799 Munich, Germany[io]
[17] Technische Universität München, Physik Department, 85748 Garching, Germany[io]
[18] Nagoya University, 464 Nagoya, Japan[n]
[19] Charles University in Prague, Faculty of Mathematics and Physics, 18000 Prague, Czech Republic[j]
[20] Czech Technical University in Prague, 16636 Prague, Czech Republic[j]
[21] State Research Center of the Russian Federation, Institute for High Energy Physics, 142281 Protvino, Russia
[22] CEA IRFU/SPhN Saclay, 91191 Gif-sur-Yvette, France
[23] Tel Aviv University, School of Physics and Astronomy, 69978 Tel Aviv, Israel[p]
[24] Trieste Section of INFN, 34127 Trieste, Italy
[25] University of Trieste, Department of Physics and Trieste Section of INFN, 34127 Trieste, Italy
[26] Abdus Salam ICTP and Trieste Section of INFN, 34127 Trieste, Italy
[27] University of Turin, Department of Physics and Torino Section of INFN, 10125 Turin, Italy
[28] Torino Section of INFN, 10125 Turin, Italy
[29] University of Eastern Piedmont, 15100 Alessandria, and Torino Section of INFN, 10125 Turin, Italy
[30] National Centre for Nuclear Research and University of Warsaw, 00-681 Warsaw, Poland[q]
[31] Warsaw University of Technology, Institute of Radioelectronics, 00-665 Warsaw, Poland[q]
[32] Yamagata University, Yamagata, 992-8510 Japan[n]

[a] Also at IST, Universidade Técnica de Lisboa, Lisbon, Portugal
[b] Supported by the DFG Research Training Group Programme 1102 “Physics at Hadron Accelerators”
[c] Also at Chubu University, Kasugai, Aichi, 487-8501 Japan[n]
[d] Also at KEK, 1-1 Oho, Tsukuba, Ibaraki, 305-0801 Japan
[e] On leave of absence from JINR Dubna
[f] present address: National Science Foundation, 4201 Wilson Boulevard, Arlington, VA 22230, United States
[g] present address: RWTH Aachen University, III. Physikalisches Institut, 52056 Aachen, Germany
[h] Also at GSI mbH, Planckstr. 1, D-64291 Darmstadt, Germany
[i] Supported by the German Bundesministerium für Bildung und Forschung
[j] Supported by Czech Republic MEYS Grants ME492 and LA242
[k] Supported by SAIL (CSR), Govt. of India
[l] Supported by CERN-RFBR Grants 08-02-91009
[m] Supported by the Portuguese FCT - Fundação para a Ciência e Tecnologia, COMPETE and QREN, Grants CERN/FP/109323/2009, CERN/FP/116376/2010 and CERN/FP/123600/2011
[n] Supported by the MEXT and the JSPS under the Grants No.18002006, No.20540299 and No.18540281; Daiko Foundation and Yamada Foundation
[o] Supported by the DFG cluster of excellence ‘Origin and Structure of the Universe’ (www.universe-cluster.de)
[p] Supported by the Israel Science Foundation, founded by the Israel Academy of Sciences and Humanities
[q] Supported by the Polish NCN Grant DEC-2011/01/M/ST2/02350
[*] Deceased

1 Introduction

The decomposition of the nucleon spin projection of 1/2 (in units of $\hbar$) into contributions from helicities and orbital angular momenta of partons became a topic of major interest in experimental and theoretical hadron physics after the European Muon Collaboration at CERN had published the surprising result that quark helicities contribute only an unexpectedly small fraction [1]. Extensive nucleon spin studies were carried out at CERN [2, 3], SLAC [4], DESY [5], JLAB [6] and at BNL [7, 8]. From the data, parton helicity distributions of the nucleon were extracted using the framework of perturbative QCD. By now, the contribution of the quark helicities to the nucleon spin is known to be about 30%, significantly smaller than the value of 60% expected from the Ellis–Jaffe sum rule [9]. Relativistic quark motion is responsible for the reduction from the value of 100%, expected in the naïve quark-parton model [10]. In spite of the ongoing theoretical debate on how to correctly perform a gauge-invariant decomposition of the nucleon spin, agreement exists that besides the contributions of the quark helicities also the gluon helicity contribution ΔG is a measurable, gauge-invariant observable (see, *e.g.* Ref. [11]).

The data of present inclusive polarised deep-inelastic scattering experiments cover a narrower range in the photon virtuality, Q^2, as compared to unpolarised ones and hence their QCD analyses (*e.g.* Ref. [12]) show only limited sensitivity to the gluon helicity distribution as a function of the gluon momentum fraction x [1], $\Delta g(x)$, and to its first moment, ΔG. Such a determination of $\Delta g(x)$ from QCD evolution has therefore to be complemented by direct, dedicated measurements.

Direct determinations of the average gluon polarisation in a limited interval of x, $\langle \Delta g/g \rangle$, were performed in a model-dependent way using the Photon-Gluon Fusion (PGF) process by SMC [13], HERMES [14] and COMPASS [15]. These analyses used events containing hadrons or hadron pairs with high transverse momenta, typically 1 to 2 GeV/c. This method provides good statistical precision but relies on Monte Carlo generators simulating QCD processes. PYTHIA [16] was used by HERMES and by COMPASS for the analysis of small Q^2 events, and LEPTO [17] by SMC and COMPASS for $Q^2 > 1$ (GeV/c)^2 events [18]. All measurements yield a small value of the gluon polarisation at $x \approx 0.1$. This is consistent with recent results from PHENIX [7] and STAR [8] at RHIC, where the production of inclusive π^0 or high transverse momentum jets led to constrain the magnitude of $\langle \Delta g/g \rangle$.

In this paper, we present new results on $\langle \Delta g/g \rangle$ and the virtual photon-nucleon asymmetries obtained from charm production tagged by D meson decays in 160 GeV/c polarised muon-nucleon scattering. The data were collected by the COMPASS Collaboration at CERN in the 2002–2004 and 2006–2007 running periods. The results supersede the ones given in Ref. [19] since they are based on the full data sample and an improved analysis method; additional final state channels are added as well. The gluon polarisation is determined assuming that open charm production is dominated by the PGF mechanism, $\gamma^* g \to c\bar{c}$, as depicted in Fig. 1. The subsequent fragmentation of the $c\bar{c}$ pair, mainly into D mesons, is assumed to be spin-independent. The dominance of the PGF mechanism in the COMPASS kinematic region is supported by the EMC results on $F_2^{c\bar{c}}$ (Ref. [20], further discussed in Ref. [21]), and by a COMPASS study of charm meson production [22]. The determination of the gluon polarisation based on this assumption, although limited statistically, has the advantage that in lowest order of the strong coupling constant there are no other contributions to the cross section.

In the present analysis, only one charmed meson is required in every event. This meson is selected through its decay in one of the following channels: $D^*(2010)^+ \to D^0\pi^+_{slow} \to (K^-\pi^+/K^-\pi^+\pi^0/K^-\pi^+\pi^+\pi^-)\pi^+_{slow}$ or $D^0 \to K^-\pi^+$, as well as their charge conjugates. The former samples are called 'tagged' ones while the latter is denoted 'untagged'. Virtual photon cross section asymmetries, $A^{\gamma N \to D^0 X}$, and the average gluon polarisation $\langle \Delta g/g \rangle$ are extracted from these open charm events. In Table 1, the kinematic variables describing the μN scattering process are listed. In this analysis we have also employed, for the first time, next-to-leading order QCD calculations for the determination of the gluon polarisation.

[1] Throughout this paper, x denotes the gluon momentum fraction, while x_B stands for the Bjorken scaling variable.

Since the PGF process is dominated by quasi-real photoproduction ($Q^2 \to 0$), the perturbative scale for the selected events, μ^2, cannot be set to Q^2 as in the QCD analyses of inclusive data. Instead, this scale is chosen to be the transverse mass of the charmed quarks, $\mu^2 \equiv 4M_{\mathrm{T}}^2 = 4(m_c^2 + p_{\mathrm{T}}^2)$, where the D meson transverse momentum, p_{T}, is defined with respect to the virtual photon.

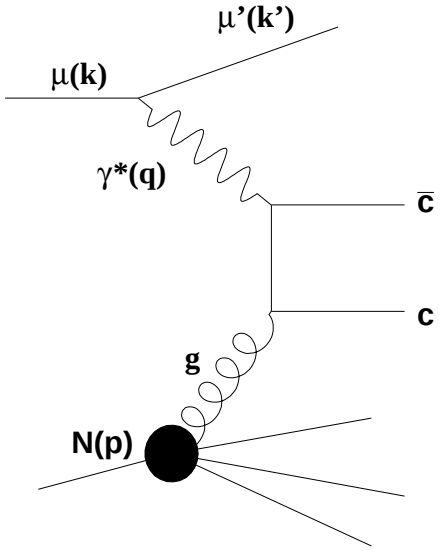

Figure 1: Photon-Gluon Fusion into a pair of charm quarks, $c\bar{c}$. Symbols in parentheses denote four-vectors.

The paper starts with a brief presentation of the experiment in Sec. 2. In Sec. 3 the data selection is reported in detail. The evaluation of the asymmetries and the corresponding results are described in Sec. 4. The determinations of the gluon polarisation $\langle \Delta g/g \rangle$ at leading (LO) and next-to-leading (NLO) QCD accuracies are presented in Sec. 5. Concluding remarks are given in Sec. 6.

2 Experimental set-up

The COMPASS spectrometer is a fixed target set-up situated at the M2 beam line of the CERN SPS using muon or hadron beams. For the present measurement, longitudinally polarised positive muons of 160 GeV/c momentum were scattered off a large polarised solid state target. A detailed description of the set-up can be found in Ref. [23].

The muons originate from the weak decay of 175 GeV/c pions and kaons produced by the 400 GeV/c SPS proton beam impinging on a primary beryllium target and are thus naturally polarised. The beam polarisation, P_μ, is about 0.8 at 160 GeV/c with a relative uncertainty of 5% [24]. A beam intensity of about $4 \cdot 10^7$ muons/s was used, with the spill length between 4.8 s and 9.6 s for SPS cycles between 16.8 s and 48 s, respectively. The beam is focused onto the target centre with a spread of 7 mm (r.m.s.) and a momentum spread of 5% for the Gaussian core. The momentum of each incoming muon is measured with a precision better than 1% upstream of the experimental hall using a beam momentum station. Before the target, the trajectory of each beam particle is determined with an angular precision of 30 μrad using a set of scintillating fibre and silicon detectors.

The solid state target is housed in a large superconducting solenoid providing a field of 2.5 T with field uniformity, $\delta B/B$, better than 10^{-4}. From 2002 to 2004, the angular acceptance was $\pm$69 mrad at the

Table 1: Kinematic variables used to describe the muon-nucleon interaction, see Fig. 1.

Variable	Symbol	Definition
Nucleon (muon) mass	$M(m_\mu)$	
Four vector of incoming (outgoing) muon	$k(k')$	
Four vector of target nucleon	p	
Four vector of outgoing hadron final state	p_X	
Four vector of virtual photon	q	$q = k - k'$
Four vector of a final state hadron	p_h	
Negative four momentum transfer squared (photon virtuality)	Q^2	$Q^2 = -q^2$
Muon laboratory incident (final) energy	$E(E')$	$E = \frac{p\cdot k}{M} \quad \left(E' = \frac{p\cdot k'}{M}\right)$
Polar angle of kaon in the D^0 centre-of-mass relative to the D^0 laboratory momentum	θ^*	
Virtual photon energy	ν	$\nu = \frac{p\cdot q}{M} \overset{\text{lab}}{=} E - E'$
Bjorken scaling variable	x_B	$x_B = \frac{Q^2}{2p\cdot q} = \frac{Q^2}{2M\nu}$
Virtual photon fractional energy	y	$y = \frac{p\cdot q}{p\cdot k} \overset{\text{lab}}{=} \frac{\nu}{E}$
Final state hadron fractional energy	z_h	$z_h = \frac{p\cdot p_h}{p\cdot q} \overset{\text{lab}}{=} \frac{E_h}{\nu}$
Transverse momentum of D^0 meson with respect to the virtual photon direction	$p_T^{D^0}$	
Energy of D^0 meson in laboratory	E_{D^0}	

upstream edge and ± 170 mrad at the downstream edge of the target material. From 2006 onwards, a new target magnet with a larger aperture solenoid was used [23]. It yields an angular acceptance of ± 180 mrad for the upstream target edge resulting in a much improved hadron acceptance and matching the ± 180 mrad acceptance of the spectrometer.

The target material consisted of ^{6}LiD beads in 2002 to 2006 and NH_3 beads in 2007, in a bath of ^{3}He -^{4}He. The target was cooled down to a temperature below 100 mK by a ^{3}He -^{4}He dilution refrigerator. The target polarisation was accomplished using the method of dynamic nuclear polarisation (DNP) and measured continuously by a set of NMR coils surrounding the target material. The achieved polarisation, P_t, was about 0.5 for deuterons (^{6}LiD) and 0.9 for protons (NH_3) with a relative uncertainty of 5% and 2%, respectively.

In 2002 to 2004, the target material was contained in two 60 cm long cells that were polarised in opposite

directions. The polarisation was reversed 3 times per day by rotating the field of the target magnet. From 2006 onwards, a three-cell target set-up was used with a central 60 cm long cell placed between two 30 cm long ones. The material inside the central cell was polarised oppositely to that of the outer ones. The use of this new target arrangement allows for further reduction of the systematic uncertainty due to the variation of the spectrometer acceptance along the target, so that only one field rotation per day was performed. In order to minimise possible acceptance effects related to the orientation of the solenoid field, also the sign of the polarisation in each target cell was reversed several times per year by changing the DNP microwave frequencies.

As not all nucleons in the target material are polarised, the so-called dilution factor, f, is introduced. It is expressed in terms of the numbers n_A of nuclei with mass number A and the corresponding total (*i.e.* including radiative effects) spin-independent cross sections, σ_A^{tot}, per nucleon for all the elements involved:

$$f_{H,D} = \frac{n_{H,D} \cdot \sigma_{H,D}^{tot}}{\Sigma_A n_A \cdot \sigma_A^{tot}}.$$

In the present analysis, the dilution factor is modified by a correction factor $\rho = \sigma_{p,d}^{1\gamma}/\sigma_{p,d}^{tot}$ accounting for the dilution due to radiative events on unpolarised protons (deuterons) [25]. A correction for polarisation of the deuteron in the ^{6}Li nucleus is also applied.

The dilution factor depends on x_B. At low x_B, it is larger for events containing hadrons in the final state due to the absence of radiative elastic tails. Its values at medium x_B for ^{6}LiD and NH_3 are about 0.37 and 0.14 with relative uncertainties of 2% and 1%, respectively .

The two stages of the COMPASS set-up are open dipole spectrometers for large and small angle tracks, respectively. Each dipole magnet is surrounded by tracking detectors. COMPASS uses various types of them in order to match the expected particle flux at various locations in the spectrometer. In high-flux regions close to the beam, tracking is provided by arrays of scintillating fibers, silicon detectors, micromesh gaseous chambers and gas electron multiplier chambers. Further away from the beam, larger-area tracking devices as multiwire proportional chambers, drift chambers and straw detectors are used. In 2006 the tracking system in the first stage of the spectrometer was adapted to match the increased aperture of the superconducting solenoid.

Muons are identified in large area tracking detectors and scintillators downstream of concrete or iron muon filters. Hadrons are detected by two scintillator-iron sandwich calorimeters installed in front of the muon filters. Electromagnetic lead glass calorimeters are placed in front of the hadron ones. The data recording system is activated by triggers indicating the presence of a scattered muon and/or energy deposited by hadrons in the calorimeters. Both inclusive and semi-inclusive triggers are used. In the former, the scattered muon is identified by coincident signals in the trigger hodoscopes, and in the latter the energy deposited in calorimeters is demanded in addition. Moreover, a calorimetric trigger with a high energy threshold is implemented to extend the acceptance. In order to suppress triggers due to halo muons, veto counters upstream of the target are used. The COMPASS trigger system covers a wide range in Q^2, from quasi-real photoproduction to the deep inelastic region.

For charged particle identification in the first stage of the set-up, a Ring Imaging Cherenkov detector (RICH) is installed [26]. It is a gas RICH with a 3 m long C_4F_{10} radiator. Two spherical mirror surfaces reflect and focus the Cherenkov photons on two sets of detectors situated above and below the acceptance of the tracking detectors, respectively. The photon detection uses MWPCs with segmented CsI photo-cathodes which detect photons in the UV region. In 2006, the central part of the RICH was upgraded replacing the MWPCs by multianode photomultiplier tubes yielding a considerably higher number of detected photons and a much faster response. For the outer parts, the readout electronics was refurbished allowing a significant reduction of the background.

The particle identification procedure relies on a likelihood function based on information on the photons

detected in the RICH and associated with a charged particle trajectory. The likelihood function uses the photons of the signal and a theoretical expectation of their distribution, taking into account possible signal losses due to dead zones in the detector. For the description of the background photons, the experimental occupancy of the photon detectors is used. For each track, likelihood values are computed for different particle mass hypotheses and the background hypothesis. Identification of a pion (kaon) is possible for momenta between 2.5 GeV/c (9 GeV/c) and 50 GeV/c.

The performance of the detectors as well as the stability of the reconstructed data was carefully monitored and all spills not fulfilling stability requirements were excluded from further analysis. Time intervals selected for asymmetry measurements correspond to periods of stable spectrometer performance. In total, data taking amounted to 48 weeks in the years 2002 to 2007.

3 Data selection

In order to extract information about the gluon polarisation, events with D mesons have to be selected from the data. This is accomplished by requiring every event containing an incoming and outgoing muon together with at least two outgoing charged tracks. Furthermore, only events with the incoming muon potentially crossing the whole target and with an interaction point (or 'vertex') within the target were retained.

The direction of tracks reconstructed at an interaction point in the target is determined with a precision better than 0.2 mrad and the momentum resolution for charged tracks detected in the first (second) spectrometer stage is about 1.2% (0.5%). The longitudinal vertex resolution varying from 5 mm to 25 mm along the target permits assigning each event to a particular target cell, *i.e.* to a specific target spin direction. In Fig. 2 are shown the distributions of the reconstructed vertex position z_{vtx} along the beam axis for events remaining after applying the aforementioned selection criteria. The relative increase of the number of events in the upstream and central target cells, seen in the right panel, reflects the acceptance increase due to the upgrade of the target magnet in 2006.

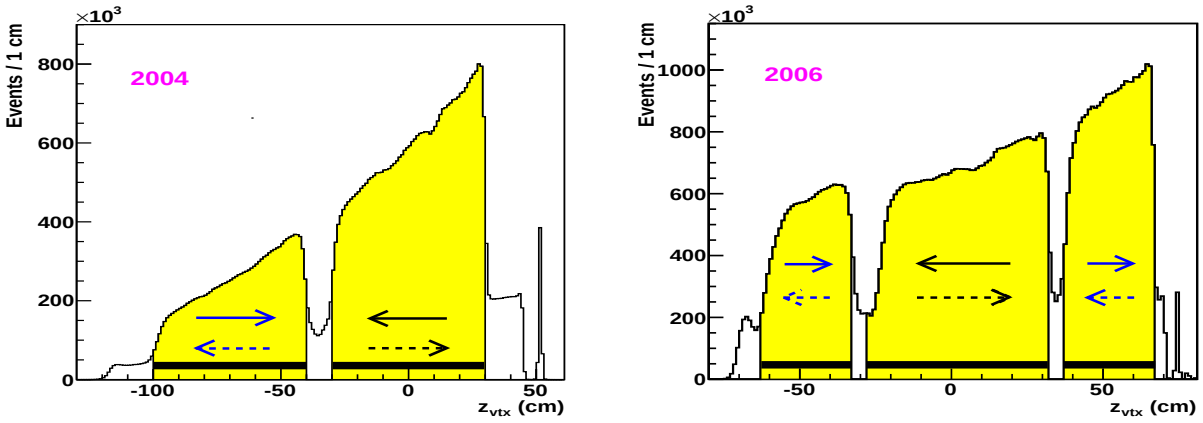

Figure 2: Distribution of reconstructed vertex positions z_{vtx} along the beam axis for the target with two (left) and three (right) cells. Dark horizontal bars at the bottom mark the target extensions, arrows denote the target polarisation directions. See text for details.

Due to multiple Coulomb scattering in the solid state target, the spatial resolution of the vertex reconstruction is not sufficient to separate production and decay points of charmed mesons. As a result, such mesons can only be reconstructed using the invariant mass of their decay products. Their decay modes considered in this analysis are listed in Table 2. Those D^0 decays which involve the same set of final state

particles cannot be distinguished event by event. Therefore five independent data samples with different final states are defined for this analysis, see Table 3. In the four tagged samples, *i.e.* $D^*_{K\pi}$, $D^*_{K_{sub}\pi}$, $D^*_{K\pi\pi^0}$, and $D^*_{K\pi\pi\pi}$, the D^0 meson is assumed to originate from a D^* decay into a D^0 meson and a slow pion, $D^* \xrightarrow{67.7\%} D^0\pi_s$. The kinematic selection criteria, which are tuned to reduce the combinatorial background without affecting the D^0 meson signal, are listed in Table 4.

Table 2: Charmed D^0 meson decay modes, together with their branching ratios, considered in this analysis. The charge conjugate (c.c.) final states from $\overline{D^0}$ decays are also included.

Reaction number	**D^0 decay mode**
1	$D^0 \xrightarrow{3.89\%} K^-\pi^+ + \text{c.c.}$
2	$D^0 \xrightarrow{13.9\%} K^-\pi^+\pi^0 + \text{c.c.}$
3	$D^0 \xrightarrow{8.09\%} K^-\pi^+\pi^+\pi^- + \text{c.c.}$

Table 3: Event samples used in the analysis. For each sample, the corresponding reactions from Table 2 are indicated. In the tagged samples, the D^0 is assumed to originate from D^* decay and the final state of the D^0 decay is indicated by the subscript where 'K_{sub}' stands for a kaon with momentum below the RICH threshold. Throughout this paper, each sample will be referred to using the above notation.

	Untagged sample	**Tagged samples**			
Sample	$D^0_{K\pi}$	$D^*_{K\pi}$	$D^*_{K_{sub}\pi}$	$D^*_{K\pi\pi^0}$	$D^*_{K\pi\pi\pi}$
Reaction number	1	1	1	2	3

Table 4: List of kinematic cuts used for each data sample. A D^0 candidate is accepted if it fullfils all conditions in a corresponding column. Here $\Delta M = M^{\text{rec}}_{K\pi\pi_s} - M^{\text{rec}}_{K\pi} - M_\pi$, where the superscript 'rec' denotes the reconstructed mass.

Variables	**Kinematic cut intervals**				
	Untagged sample	**Tagged samples**			
	$D^0_{K\pi}$	$\mathbf{D^*_{K\pi}}$	$\mathbf{D^*_{K\pi\pi^0}}$	$\mathbf{D^*_{K_{sub}\pi}}$	$\mathbf{D^*_{K\pi\pi\pi}}$
$(M^{\text{rec}}_{K\pi} - M_{D^0})$ [MeV/c^2]	$[-400,\ +400]$	$[-600,\ +600]$		$[-400,\ +400]$	
$\lvert\cos\theta^*\rvert$	< 0.65	< 0.90		< 0.85	
z_{D^0}	$[0.20,\ 0.85]$	$[0.20,\ 0.85]$		$[0.25,\ 0.85]$	$[0.30,\ 0.85]$
p_K [GeV/c]	$[9.5,\ 50]$	$[9.5,\ 50]$		$[2.5,\ 9.5]$	$[9.5,\ 50]$
p_π [GeV/c]	$[7,\ 50]$	$[2.5,\ 50]$			
ΔM [MeV/c^2]	—	$[3.2, 8.9]$			$[4.0, 7.5]$
p_{π_s}[GeV/c]	—	< 8			

Particles are identified using the RICH detector. Using the measured momentum of a charged particle and the distributions of Cherenkov photons, likelihood values for different mass hypotheses and for the

background hypothesis are computed. A particle is identified as kaon or pion if the likelihood value is larger than those for all remaining hypotheses. This procedure is very efficient in reducing the combinatorial background of two particles other than π and K. A detailed description of the identification procedure is given in Ref. [27].

The following selection criteria were applied to obtain the final event samples. The untagged sample $\mathrm{D}^0_{\mathrm{K}\pi}$ contains events with Kπ pairs in the reconstructed mass range given in Table 4, which do not stem from decays of reconstructed D^* mesons, see Fig. 3. Due to large combinatorial background this sample requires more restrictive cuts for the identification of pion and kaon: a pion momentum above 7 GeV/c is required to avoid contamination from electrons. For the four tagged samples, a D^* meson is selected by requiring the presence of a slow pion, $p_{\pi_\mathrm{s}} < 8$ GeV/c, in addition to a D^0 candidate. The presence of the slow pion permits the application of two additional cuts. The first one uses the RICH detector to reject electrons that mimic slow pion candidates and reduces the combinatorial background by a factor of two. The second one is a cut on the mass difference, $\Delta M = M^{\mathrm{rec}}_{\mathrm{K}\pi\pi_\mathrm{s}} - M^{\mathrm{rec}}_{\mathrm{K}\pi} - M_\pi$, where $M^{\mathrm{rec}}_{\mathrm{K}\pi\pi_\mathrm{s}}$ and $M^{\mathrm{rec}}_{\mathrm{K}\pi}$ are the reconstructed masses of the D^* and the D^0 candidates, respectively. This mass difference can be measured with very good precision and thus the cut on ΔM results in a significant reduction of the combinatorial background in the tagged samples.

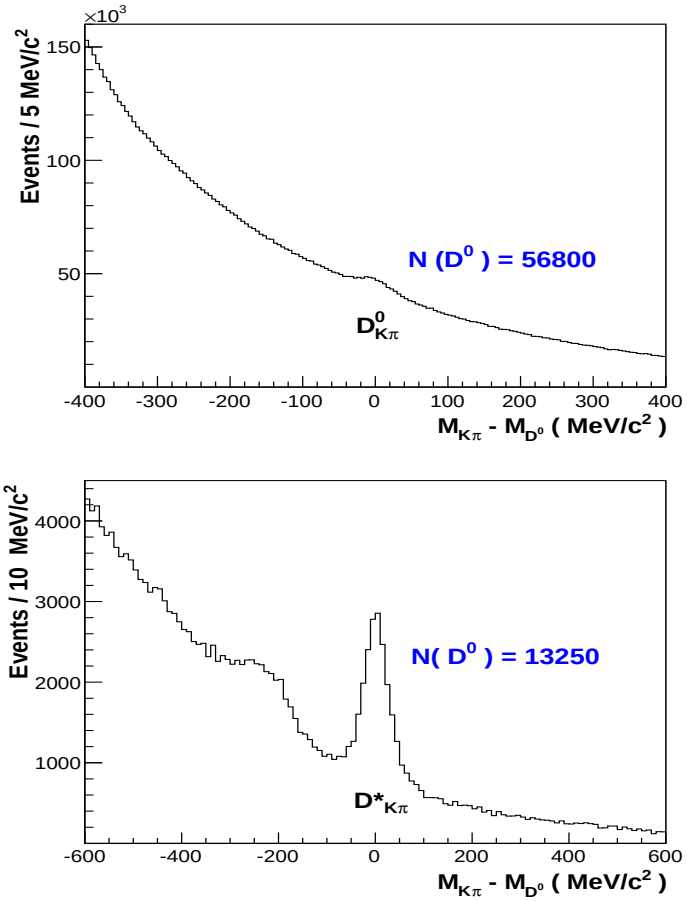

Figure 3: Invariant mass spectra for the $\mathrm{D}^0_{\mathrm{K}\pi}$ and $\mathrm{D}^*_{\mathrm{K}\pi}$ samples with the approximate number of D^0 mesons above background.

In addition to the cuts described above, further kinematic cuts were applied to all samples. It is demanded that $|\cos\theta^*| < 0.9$ for the tagged $\mathrm{D}^*_{\mathrm{K}\pi}$ and $\mathrm{D}^*_{\mathrm{K}\pi\pi^0}$ samples, $|\cos\theta^*| < 0.65$ for the sample $\mathrm{D}^0_{\mathrm{K}\pi}$ and $|\cos\theta^*| < 0.85$ for the remaining samples. This cut suppresses mainly background events and improves the significance of the signal. Finally, all events have to satisfy a cut on z_{D^0}. Since a pair of

charmed quarks is produced in the centre-of-mass of the $\gamma^* g$ system, each quark receives on average half of the virtual photon energy. Indeed, the measured z_{D^0} distribution and the one simulated assuming a pure PGF process (with parton showers included) are very similar and have a most probable value close to 0.5, see Fig. 4. This fact strongly supports the assumption on PGF dominance in charm production.

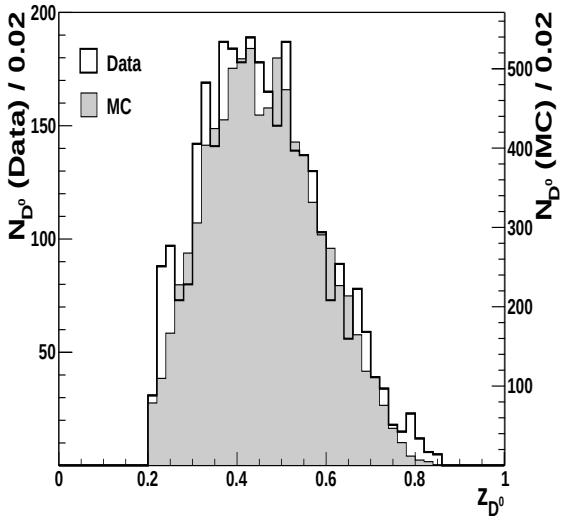

Figure 4: Distribution of z_{D^0} for the $D^*_{K\pi}$ data sample (background is subtracted) and corresponding Monte Carlo events. D^0 mesons are selected in the ± 80 MeV/c^2 mass window around the D^0 mass.

Final mass spectra for the untagged and tagged samples, selected according to kinematic cuts listed in Table 4, are shown in Fig. 3. For the latter, a most pronounced signal is visible at the D^0 mass with a mass resolution of about 27 MeV/c^2. In this mass spectrum, also a second structure is visible at about –250 MeV/c^2 which is due to events with $D^0 \longrightarrow K^-\pi^+\pi^0$ decays with neutral pion not reconstructed in the analysis. Thus the $K\pi$ spectrum is shifted to lower mass as compared to $D^0 \longrightarrow K^-\pi^+$ decays. The purity of this signal is much worse due to the non-reconstructed neutral pion.

Further improvement of the significance of the signal is accomplished by applying the Neural Network method described in Sec. 4.1.2 which leads to a considerable reduction of the combinatorial background in the tagged samples. The resulting mass spectrum for $D^*_{K\pi\pi^0}$ is shown in Fig. 5, with an improvement of the signal strength by 15% while for the $D^0 \longrightarrow K^-\pi^+$ the signal and the background are reduced in a similar way so that the significance of the signal stays unchanged. Therefore only the criteria from Table 4 are used to select the final $D^*_{K\pi}$ sample, see Fig. 3.

Results on channels with a weaker D^0 signal like $D^*_{K\pi\pi\pi}$ and $D^*_{K_{sub}\pi}$, are also shown in Fig. 5. The sample $D^*_{K_{sub}\pi}$ contains events where the momentum of the kaon candidate is below the limit of 9 GeV/c for kaon identification by the RICH detector. Simulations using a Monte Carlo generator for heavy flavours, AROMA [28], and a full spectrometer description based on GEANT [29] have shown that about 30% of the kaons coming from D^0 decays have their momenta below this RICH threshold. Therefore it is only required that those particles, K_{sub}, are not identified as pions or electrons.

In the case the two D^0 candidates are found in the same event, only one of them, chosen randomly, is considered in the analysis. If two channels contribute with a D^0 candidate to the same event, only one of them is accepted according to the following priority rule: $D^*_{K\pi\pi\pi}$, $D^*_{K\pi}$ or $D^*_{K\pi\pi^0}$, $D^0_{K\pi}$, $D^*_{K_{sub}\pi}$ (see Ref. [27]).

Distributions of x_B, Q^2 and y variables for the $D^*_{K\pi}$ candidates from 2006, and from the D^0 signal region,

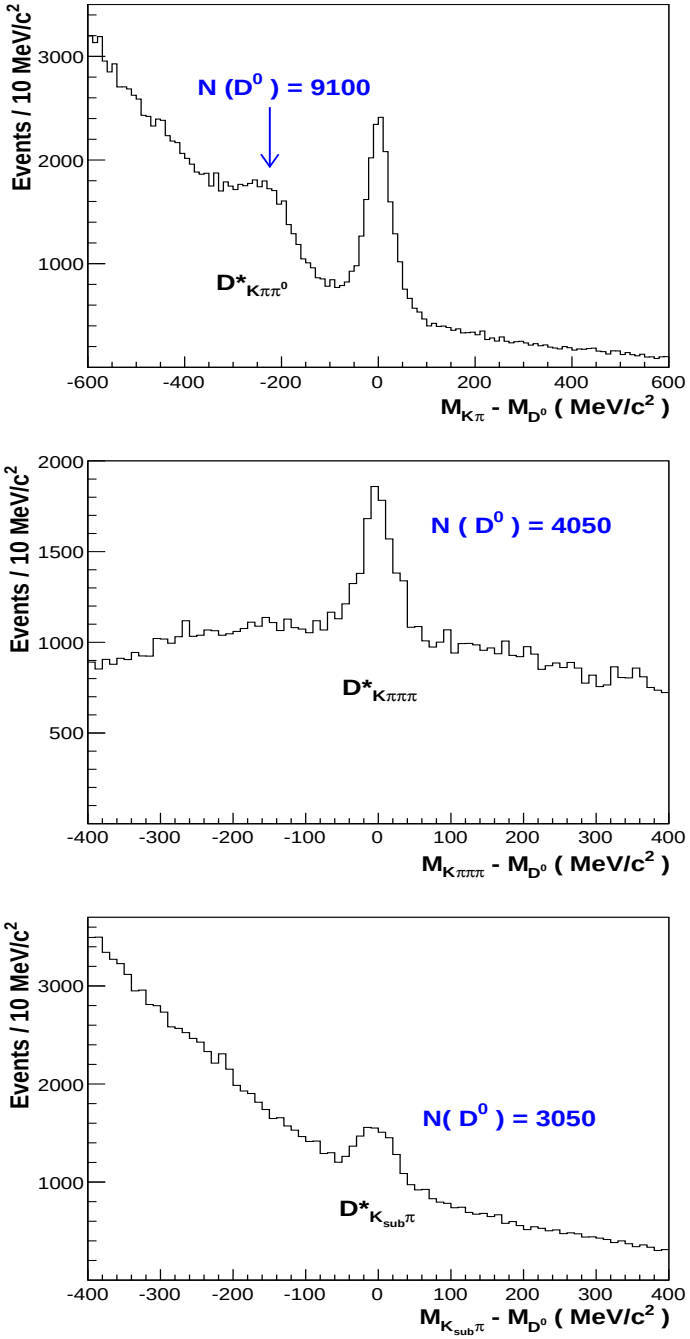

Figure 5: Invariant mass spectra for the $D^*_{K\pi\pi^0}$, $D^*_{K\pi\pi\pi}$ and $D^*_{K_{sub}\pi}$ samples. The purity of the samples was improved using the Neural Network. The approximate number of D^0 mesons above background is given.

are presented in Fig. 6. For those events x_B values range from about 10^{-5} to 0.1 with $\langle x_B \rangle = 0.004$, Q^2 values from 10^{-3} to 30 (GeV/c)^2 with $\langle Q^2 \rangle = 0.6$ (GeV/c)^2, and y values from 0.1 to 1 with $\langle y \rangle = 0.63$.

4 Asymmetry evaluation

In this section, we describe the determination of the virtual photon asymmetry for D^0 production, $A^{\gamma N} \equiv A^{\gamma N \to D^0 X}$, from the event samples defined in Table 3. The method is similar to the one used

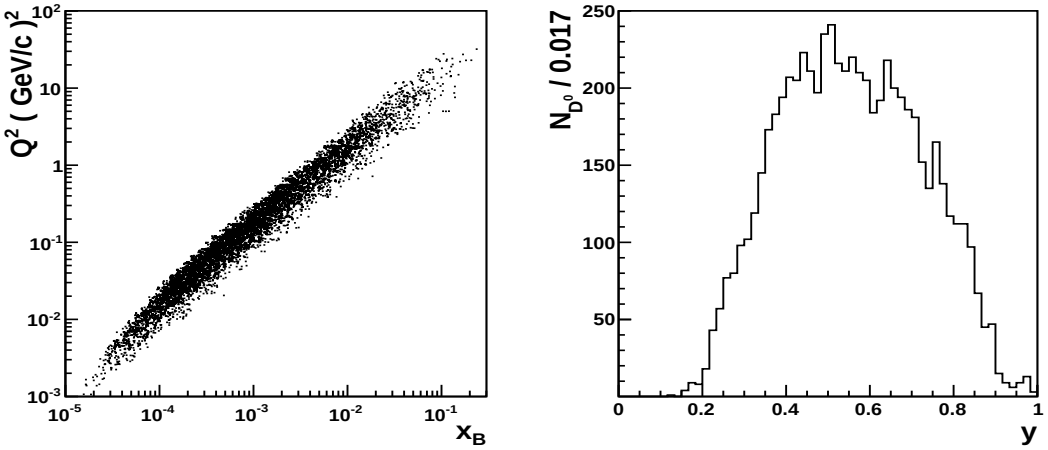

Figure 6: A scatter plot of Q^2 *vs* x_B and a distribution of y for the 2006 $D^*_{K\pi}$ sample selected as in Fig. 4 except that the background is not subtracted.

in our previous publication [19]. The asymmetry $A^{\gamma N}$ can be used in various ways to evaluate the gluon polarisation $\langle \Delta g/g \rangle$ at LO or NLO QCD accuracy.

4.1 Analysis method

4.1.1 Asymmetries

The number of events collected in a given target cell and time interval is given by:

$$\frac{\mathrm{d}^k N}{\mathrm{d}m\,\mathrm{d}X} = a\phi n(s+b)\left[1 + P_t P_\mu f\left(\frac{s}{s+b}A^{\mu N\to\mu' D^0 X} + \frac{b}{s+b}A_B\right)\right]. \tag{1}$$

Here, $A^{\mu N\to\mu' D^0 X}$ is the longitudinal double spin asymmetry of the differential cross section for events with a D^0 or $\overline{D^0}$ in the final state, and A_B is the corresponding asymmetry originating from background events. Furthermore, $m \equiv M_{K\pi}$ (or $m \equiv M_{K\pi\pi\pi}$) and the symbol X denotes a set of $k-1$ kinematic variables describing an event ($p_T^{D^0}$, E_{D^0}, Q^2, y, ...), while a, ϕ and n are the spectrometer acceptance, the incident muon flux integrated over the time interval, and the number of target nucleons respectively. The differential unpolarised cross sections for signal and background, folded with the experimental resolution as a function of m and X, are represented by $s = s(m,X)$ and $b = b(m,X)$ respectively. The ratio $s/(s+b)$ will be called 'signal purity' and the ratio $b/(s+b)$ 'background purity'. The information on the gluon polarisation is contained in the virtual photon asymmetry $A^{\gamma N} = A^{\mu N\to\mu' D^0 X}/D$. Similarly, the background asymmetry can be written as $A_B^{\gamma N} = A_B/D$. Here, D is the so-called depolarisation factor accounting for the polarisation transfer from lepton to virtual photon:

$$D = \frac{y\left[2 - y - \frac{2y^2 m_\mu^2}{Q^2}\right]}{y^2\left(1 - \frac{2m_\mu^2}{Q^2}\right) + 2(1-y)}. \tag{2}$$

A straightforward way to extract $A^{\gamma N}$ would be the following: Eq. (1) is integrated over the variables X to obtain the number of events in both spin configurations as a function of the invariant mass m. Next, the event number asymmetry in the D^0 signal region is extracted, and a possible background asymmetry, determined from the asymmetries in sidebands to the left and right from the signal region, is subtracted.

For this analysis, however, we choose the method of event weighting, which is advantageous in terms of statistical precision. Compared to previous COMPASS analyses where weighting procedures were

applied [3], here the weighting procedure is extended to determine the background asymmetry $A_{\mathrm{B}}^{\gamma\mathrm{N}}$ simultaneously with $A^{\gamma\mathrm{N}}$ [30]. In order to achieve this, every event is weighted once with a signal weight, w_{S}, and once with a background weight, w_{B}:

$$w_{\mathrm{S}} = P_\mu f D \frac{s}{s+b}, \tag{3}$$

$$w_{\mathrm{B}} = P_\mu f D \frac{b}{s+b}. \tag{4}$$

Except for the target polarisation P_{t}, these weights are the prefactors of the asymmetries $A^{\gamma\mathrm{N}}$ and $A_{\mathrm{B}}^{\gamma\mathrm{N}}$, see Eq. (1). The target polarisation is not included in the weights because its time dependence would lead to an increase in false asymmetries. The signal and background purities are included in the respective weights. This procedure leads to the highest possible statistical precision which would also be obtained in the unbinned maximum likelihood method [30, 31]. Note that the unbinned maximum likelihood method, cannot be applied here because the acceptance and flux factors in Eq. (1) are not known with sufficient precision, only their ratios for different spin states and target cells are known. These ratios will be used for the extraction of $A^{\gamma N}$ and $A_{\mathrm{B}}^{\gamma N}$.

The asymmetry $A^{\gamma\mathrm{N}}$ is extracted in bins of D^0 transverse momentum with respect to the virtual photon, $p_{\mathrm{T}}^{\mathrm{D}^0}$, and D^0 energy in the laboratory system, E_{D^0}. These variables and their binning were chosen to minimise the influence of the experimental acceptance on the asymmetry. As $A^{\gamma\mathrm{N}}$ does not contain the depolarisation factor D, its remaining dependence on the inclusive variables y and Q^2 is very weak. The expectation value of the sum of signal weights is obtained as:

$$\begin{aligned}\left\langle \sum_{i=1}^{N_t} w_{\mathrm{S},i} \right\rangle &= \int w_{\mathrm{S}}(X,m)\, \frac{\mathrm{d}^k N_t}{\mathrm{d}m\,\mathrm{d}X} \mathrm{d}m\mathrm{d}X \\ &= \alpha_{\mathrm{S},t} \left[1 + \langle \beta_{\mathrm{S}} \rangle_{w_{\mathrm{S}}} \left\langle A^{\gamma\mathrm{N}} \right\rangle_{w_{\mathrm{S}}\beta_{\mathrm{S}}} + \langle \beta_{\mathrm{B}} \rangle_{w_{\mathrm{S}}} \left\langle A_{\mathrm{B}}^{\gamma N} \right\rangle_{w_{\mathrm{S}}\beta_{\mathrm{B}}} \right]. \end{aligned} \tag{5}$$

The symbols used are defined as:

$$\alpha_{\mathrm{S},t} = \int w_{\mathrm{S}}\; a_t\; \phi_t\; n_t\; (s+b)\; \mathrm{d}m\; \mathrm{d}X, \tag{6}$$

$$\langle \eta \rangle_w = \frac{\int \eta w a_t \phi_t n_t (s+b) \mathrm{d}m \mathrm{d}X}{\int w a_t \phi_t n_t (s+b) \mathrm{d}m \mathrm{d}X}, \tag{7}$$

with $\beta_{\mathrm{S}} = w_{\mathrm{S}} P_{\mathrm{t}}$, $\beta_{\mathrm{B}} = w_{\mathrm{B}} P_{\mathrm{t}}$, $\eta \in \left[\beta_{\mathrm{S}}, \beta_{\mathrm{B}}, A^{\gamma\mathrm{N}}, A_{\mathrm{B}}^{\gamma\mathrm{N}}\right]$ and $w \in [w_{\mathrm{S}}, w_{\mathrm{B}}, w_{\mathrm{S}}\beta_{\mathrm{S}}, w_{\mathrm{S}}\beta_{\mathrm{B}}]$. The index t denotes the target cell before ($t = u, d$) or after ($t = u', d'$) spin rotation and N_t is the number of events observed in a given target cell[2]. An equation analogous to Eq. (5) holds for the sum of background weights $\langle \sum_{i=1}^{N_t} w_{\mathrm{B},i} \rangle$, with analogous definition of symbols. In total, eight equations similar to Eq. (5) are obtained for every $(p_{\mathrm{T}}^{\mathrm{D}^0}, E_{\mathrm{D}^0})$ bin: for the signal and background weights in two target cells and for two spin configurations. These eight equations contain 12 unknowns: $\langle A^{\gamma\mathrm{N}} \rangle_{w_{\mathrm{S}}\beta_{\mathrm{S}}}$, $\langle A_{\mathrm{B}}^{\gamma\mathrm{N}} \rangle_{w_{\mathrm{S}}\beta_{\mathrm{B}}}$, $\langle A^{\gamma\mathrm{N}} \rangle_{w_{\mathrm{B}}\beta_{\mathrm{S}}}$, $\langle A_{\mathrm{B}}^{\gamma\mathrm{N}} \rangle_{w_{\mathrm{B}}\beta_{\mathrm{B}}}$, four acceptance factors $\alpha_{\mathrm{S,t}}$ and four acceptance factors $\alpha_{\mathrm{B,t}}$.

The expectation values of the sum of weights on the left hand side of Eq. (5) are identified with the measured sums of weights. In order to extract $A^{\gamma\mathrm{N}}$ and $A_{\mathrm{B}}^{\gamma\mathrm{N}}$ from the measured sums of weights one proceeds as follows. The factors $\langle \beta_{\mathrm{S,B}} \rangle_{w_{\mathrm{S}}, w_{\mathrm{B}}}$ are evaluated from data, *e.g.*

$$\langle \beta_{\mathrm{S}} \rangle_{w_{\mathrm{S}}} \approx \frac{\sum_{i=1}^{N_t} \beta_{\mathrm{S}} w_{\mathrm{S}}}{\sum_{i=1}^{N_t} w_{\mathrm{S}}}. \tag{8}$$

[2] In 2006–2007 d and u stand for the central target cell and the sum of the outer ones, respectively.

The expectation values appearing in Eq. (7) contain the spin-averaged cross section while the sum over events in Eq. (8) used to evaluate these expectation values runs over the spin-dependent events. This has a negligible effect on the result because the raw asymmetry $P_t P_\mu f D \langle A^{\gamma N} \rangle$ is very small. This smallness makes sure that neither the result nor its statistical error are sensitive to the fact that the same data which are used to determine the asymmetries are also used to evaluate the expectation values above.

The acceptance factors $\alpha_{S,t}$ and $\alpha_{B,t}$ cannot be determined with sufficient precision to extract $A^{\gamma N}$ and $A_B^{\gamma N}$ directly from the set of eight equations. By assuming that for both signal and background possible acceptance variations affect the upstream and downstream cells in the same way, *i.e.* $\alpha^u/\alpha^d = \alpha^{u'}/\alpha^{d'}$, the number of unknowns is reduced to ten. With an extra, much weaker assumption that signal and background events from the same target cell are affected in the same way by the acceptance variations, one arrives at a system of eight equations with nine unknowns. Possible deviations from the above assumptions may generate false asymmetries which are included in the systematic uncertainty, see Sec. 5.1.

The number of unknowns is reduced to seven with two additional assumptions:

$$\left\langle A^{\gamma N} \right\rangle_{w_S \beta_S} = \left\langle A^{\gamma N} \right\rangle_{w_B \beta_S} = A^{\gamma N} \quad \text{and} \quad \left\langle A_B^{\gamma N} \right\rangle_{w_S \beta_B} = \left\langle A_B^{\gamma N} \right\rangle_{w_B \beta_B} = A_B^{\gamma N}, \tag{9}$$

which are satisfied for constant values of $A^{\gamma N}$ and $A_B^{\gamma N}$ in a given bin. The uncertainty on the gluon polarisation introduced by this assumption will be discussed in Sec. 5.2. Using the set of eight equations, the asymmetry $A^{\gamma N}$ and the background asymmetry $A_B^{\gamma N}$ are determined simultaneously by a standard least square minimisation procedure, which takes into account the statistical correlation between $\sum w_S$ and $\sum w_B$ in the same target cell. The correlation factor $\mathrm{cov}\left(\sum w_S, \sum w_B\right)$ is given in Ref. [31]. The analysis is performed independently for each $(p_T^{D^0}, E_{D^0})$ bin and D meson decay channel.

For determinations of average values of kinematic variables in each $(p_T^{D^0}, E_{D^0})$ bin, a weight equal to w_S^2 is used, in accordance with Eq. (5).

4.1.2 The signal purity

The signal purity $s/(s+b)$ can be extracted from a fit to the invariant mass distribution of D^0 candidates. It depends on kinematic variables, for instance it is large at high transverse momenta $p_T^{D^0}$ of the $K\pi$ system and small at low $p_T^{D^0}$. In order to implement the kinematic dependence of the signal purity in the weights given by Eqs (3, 4), one would naively proceed by performing fits to the corresponding invariant mass distributions in bins of kinematic variables. This procedure is not feasible in our case because of limited statistics. Instead, in this analysis a classification based on a Neural Network is employed [27].

Here, the aim of the Neural Network is to distinguish signal from background events using only data. The network consists of information processors (neurons), which are interconnected and organized into layers. The external information fed into the input layer is processed in the hidden layers and the result produced by the output layer is a classification of the event by the network. In the present case, the input layer contains a set of kinematic observables: ratios of RICH likelihoods, $\cos\theta^*$, z_D and kaon momentum. There are two hidden layers and the number of neurons in them varies during the training process (dynamic network). For each event, the network tunes the strength of each variable-neuron and neuron-neuron connection. The strengths are obtained by minimising the squared deviation between the expected output and the actual Neural Network prediction. This training process stops when the deviation reaches a stable minimum [32].

For each event sample (see Table 3), two data sets are used as inputs to the Neural Network. The first one contains the D^0 signal and the combinatorial background events. These events are called 'good charge combination' ones (*gcc*) referring to the charges of particles from D^0 decays, and they are selected as described in Sec. 3. The second set, the 'wrong charge combination' events (*wcc*), is selected in a

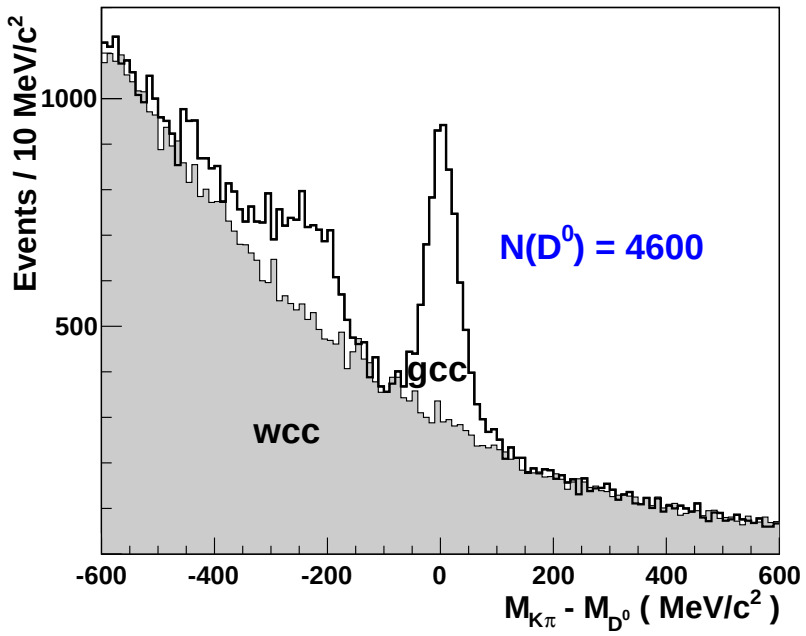

Figure 7: Example of the Kπ invariant mass spectrum for the $D^*_{K\pi}$ sample with good (*gcc*) and wrong (*wcc*) combination of pion and kaon charge signs. See text for details. Data were collected in 2007 with the proton (NH_3) target.

similar way except that the sum of charges of corresponding particles should not be zero. It contains only background events and is used as a background model (see Fig. 7). The Neural Network performs a multi-dimensional comparison of *gcc* and *wcc* events in a ± 40 MeV/c^2 mass window around the D^0 mass[3]. Within the *gcc* set, signal events are distinguished from combinatorial background by exploiting differences between the *gcc* and *wcc* sets in the shapes of distributions of kinematic variables as well as multi-dimensional correlations between them. An example of a properly chosen variable for the network is $\cos\theta^*$, as shown in Fig. 8. The reconstructed mass cannot be used because it would enhance the probability of a background event in the signal region to be a true D meson.

The network classifies all the *gcc* events according to their similarity in kinematics with respect to the *wcc* ones, and to each event it assigns a probability of being a signal. A probability of 0.5 is assigned to indistinguishable events. If the network is trained with proper input samples, *i.e.* a correct background model and a sufficiently strong signal, the network output, $[s/(s+b)]_{\rm NN}$, can be directly interpreted as an estimate of the signal purity in the corresponding mass window. This is the so called 'pure' Neural Network method, applicable to the $D^*_{K\pi\pi^0}$, $D^*_{K\pi}$ and $D^*_{K\pi\pi\pi}$ samples collected in 2004–2007, where event statistics and signal purities are large.

The mass dependence of signal and background strengths, $s(m)$ and $b(m)$, which cannot be obtained from the Neural Network in an unbiased way, is determined from a fit to the mass spectra in bins of $[s/(s+b)]_{\rm NN}$. In order to describe the signal a Gaussian distribution is used for all samples, while for the background the following fitting functions are employed: two exponential distributions for the $D^0_{K\pi}$ channel and one exponential for the D^* tagged channels. An exception is the $D^*_{K\pi\pi\pi}$ sample, for which a second degree polynomial is used. From those fits, corrections λ to the signal purity are obtained in the mass windows defined above:

[3] A mass window of ± 30 MeV/c^2 is used for the sample $D^0_{K\pi}$ and ± 40 MeV/c^2 around -250 MeV/c^2 for the sample $D^*_{K\pi\pi^0}$.

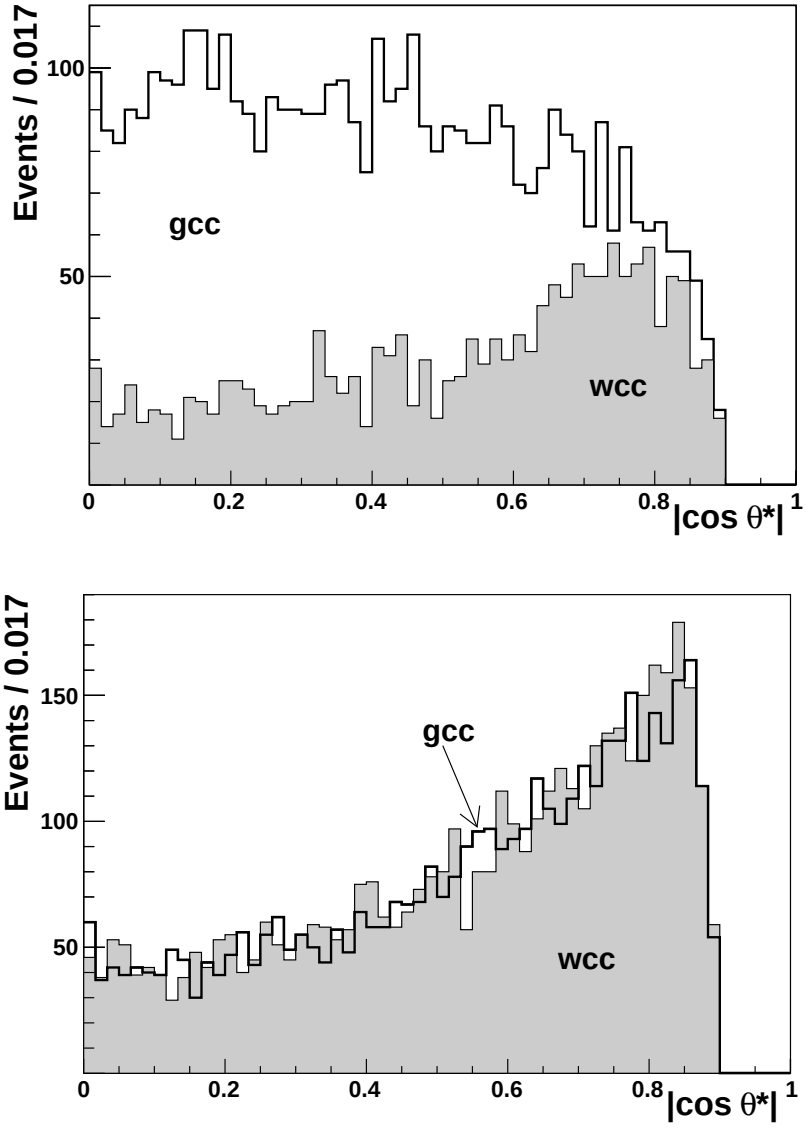

Figure 8: Example of the distribution of $|\cos\theta^*|$ (polar angle of kaon in the D^0 centre-of-mass relative to the D^0 momentum) in the D^0 meson rest frame for the *gcc* and *wcc* events ($D^*_{K\pi}$ sample, 2006 data). Top: region of the D^0 signal, bottom: outside the D^0 signal.

$$\lambda = \left\langle \left(\frac{s}{b}\right)_{\mathrm{NN}} \right\rangle \frac{\int b(m)\mathrm{d}m}{\int s(m)\mathrm{d}m}\,, \tag{10}$$

so that

$$\frac{s}{s+b} = \frac{\lambda s(m)}{\lambda s(m) + b(m)}. \tag{11}$$

The fit of the invariant mass spectra in bins of the NN signal purity can also be used to validate the classification obtained by the Neural Network. For each bin, the signal purity is determined from an integration of the signal and background fits over the mass windows used. Good agreement between signal purities from the NN and the fit is found for all samples, which confirms that the Neural Network

does not introduce any bias in the analysis. As an illustration, the mass spectra in bins of the NN signal purity together with a comparison of the two signal purities are shown for the $D^*_{K\pi}$ sample in Fig. 9. The signal purity clearly increases with increasing $[s/(s+b)]_{NN}$. Equally good agreement is found when comparing $s/(s+b)$ between NN and data in bins of $(p_T^{D^0}, E_{D^0})$.

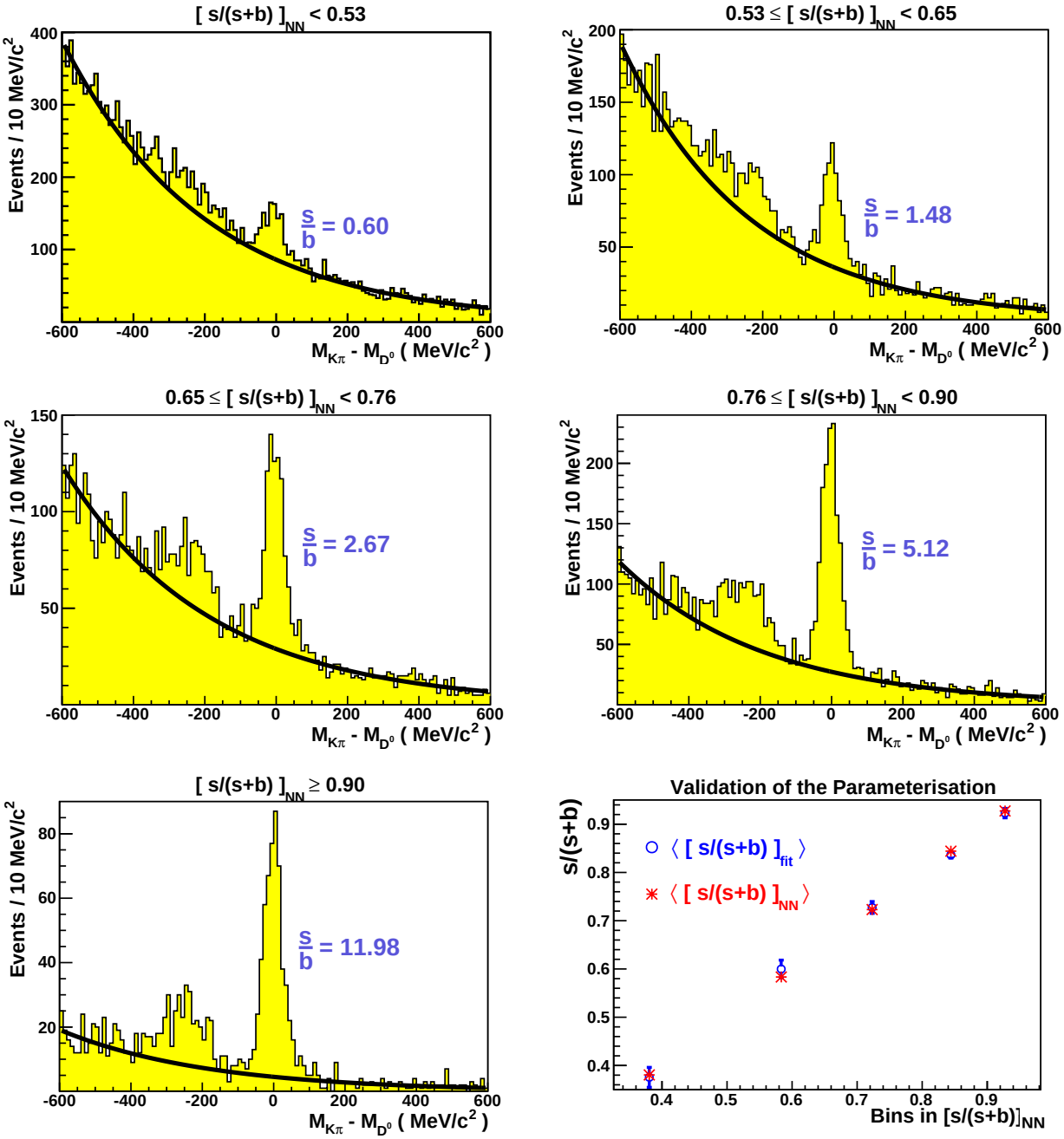

Figure 9: The Kπ invariant mass spectra in bins of the NN signal purity $[s/(s+b)]_{NN}$ for the $D^*_{K\pi}$ sample. The last panel shows a comparison of the two purities, $[s/(s+b)]_{NN}$ and $[s/(s+b)]_{fit}$ (see text for details). Curves show the background component of the invariant mass fits described in the text. The significance of the $D^*_{K\pi}$ signal is shown as ratio s/b.

The signal purity can be parameterised in various ways provided it correctly reproduces the data. Several parameterisations were found to indeed yield asymmetries compatible within statistical uncertainties. In order to achieve the statistically most precise result on the gluon polarisation, we chose the method

described in Sec. 5.2. As a special feature in this method the signal weight contains the product of the signal purity and $a_{\rm LL}$, which is the partonic asymmetry for the PGF process. Observation shows that $a_{\rm LL}$ is strongly anticorrelated with the signal purity. Therefore a parameterisation of $a_{\rm LL}$, validated as described in Ref. [27], was additionally included in the training of the NN.

For the low purity sample $\mathrm{D}^0_{\mathrm{K}\pi}$ collected in 2002–2007, and for all samples collected in 2002 and 2003, the extraction of the signal purities from the network is more complicated since the anticorrelation mentioned above cannot be accounted for because of weak signals. Therefore a 'hybrid' method is employed. Similar to the method used in Refs [19, 33], this approach uses fits to the mass spectra which are sampled in bins of two variables, NN signal purity (from a parameterisation without $a_{\rm LL}$ in the training) and $fP_\mu a_{\rm LL}$. The former sorts the events according to their similar kinematic dependences, while the latter is used to ensure the anticorrelation between $a_{\rm LL}$ and the signal purity. The signal and background distributions belonging to the mass spectra sampled in the bins are fitted by the same fitting functions as defined above for describing the mass dependence of signal and background. Integrating the fits within the same mass windows as used for the NN training procedure yields the signal purities extracted from the fit. For each of the two variables, a function is built using linear interpolations between the fit results. An iterative procedure is used to obtain a stable result on these two functions simultaneously, and thereafter the correction λ is applied to the signal purity. Due to the statistical limitations, only one parameterisation was built for each decay channel and year.

As the hybrid method can be used for both, low purity and high purity channels, it was decided to use it for all parametrisations of signal purities. Although more complex than the pure NN method, the hybrid method results in a comparable statistical precision.

4.2 Results on asymmetries

The asymmetry $A^{\gamma\mathrm{N}}$ is extracted simultaneously with the background asymmetry $A_{\rm B}^{\gamma\mathrm{N}}$ for each bin, channel, and year of data taking except for low purity channels where some data taking years of the same target set-up are merged. Final results sorted by D^0 decay mode are shown in Tables 5 – 7, where $A^{\gamma\mathrm{N}}$ is given in each $(p_{\rm T}^{\mathrm{D}^0}, E_{\mathrm{D}^0})$ bin together with average values of kinematic variables. All averages are calculated with the weight $w_{\rm S}^2$. The muon-nucleon asymmetry $A^{\mu\mathrm{N}\to\mu'\mathrm{D}^0\mathrm{X}}$ can be obtained from $A^{\gamma\mathrm{N}}$ by multiplying it by $\langle D\rangle$, which is a function of $\langle y\rangle$ and $\langle Q^2\rangle$ and is also given in Tables 5 – 7.

As the extraction of $A^{\gamma\mathrm{N}}$ is performed based on event weights, uncertainties introduced into the determination of the asymmetry by each contribution to the weight have to be accounted for. The uncertainty of $A^{\gamma\mathrm{N}}$ is acquired from a spread of weighting factors w, Eq. (3), which is obtained by comparing the default analysis with weight w_0 to other analyses with different weight, w. The expectation value of the weighted asymmetry is $\langle A^{\gamma\mathrm{N}}_{w_0}\rangle = \langle ww_0\rangle/\langle w_0^2\rangle A^{\gamma\mathrm{N}}$, as shown in Ref. [27]. The spread of $\langle ww_0\rangle/\langle w_0^2\rangle$ gives the relative systematic uncertainty of $A^{\gamma\mathrm{N}}$.

The major sources of systematic uncertainties in the measurement of $A^{\gamma\mathrm{N}}$ are discussed below. The contributions from P_μ, $P_{\rm t}$ and f are taken conservatively as 5%, 5% and 2% respectively, for both deuteron and proton targets. In order to study the contribution of $s/(s+b)$ to the systematic uncertainty, three tests are performed. In one of them, different fitting functions are used for the functional form of the background. In the other two, different mass windows are investigated concerning the Neural Network parameterisation and the choice of the binning used in the reconstruction of the D^0 spectra. Note that each of these tests leads to several new values of $s/(s+b)$ and, consequently, new weights w are obtained. The resulting spread of weights is computed for each year of data taking, each sample and each bin with respect to the default weight w_0. Thereafter, the weighted average of all spreads is determined separately for each of the three systematic tests considered. The combined uncertainty on $s/(s+b)$ is obtained from a quadratic superposition of these three uncertainties. The resulting average value over all bins is 7% of the measured asymmetries.

The contribution of D to the uncertainty of $A^{\gamma N}$ is obtained as follows. According to the experimental uncertainty of 1% in the measurement of the mean value of the scattered muon momentum, shifted values of y are calculated for every event. Thereafter, new values of D are computed from Eq. (2). The resulting spread of $\langle ww_0\rangle/\langle w_0^2\rangle$ gives a systematic uncertainty of 1.6%.

Systematic uncertainties of $A^{\gamma N}$ arising from false asymmetries and from the assumptions specified in Eq. (9) can be best estimated using the statistically optimised method (see Sec. 5.2). First, they are determined for the gluon polarisation $\Delta g/g$, and then they are translated to $A^{\gamma N}$ in bins of $(p_T^{D^0}, E_{D^0})$ employing $\langle a_{LL}/D\rangle$. Averaging over all bins, the resulting absolute values of the uncertainties due to false asymmetries and the assumptions in Eq. (9) are 0.022 and 0.007, respectively.

The total systematic uncertainties of $A^{\gamma N}$, as given in Tables 5 – 7, are obtained by adding all contributions in quadrature.

Table 5: Combined asymmetries $A^{\gamma N\to D^0 X}$ for the $D^0_{K\pi}$, $D^*_{K\pi}$ and $D^*_{K_{sub}\pi}$ samples in bins of ($p_T^{D^0}$, E_{D^0}), together with the weighted (with w_S^2) averages of several kinematic variables. First uncertainty is statistical, second is systematic.

Bin limits		$A^{\gamma N\to D^0 X}$	$\langle y\rangle$	$\langle Q^2\rangle$	$\langle p_T^{D^0}\rangle$	$\langle E_{D^0}\rangle$	$\langle D\rangle$
$p_T^{D^0}$ (GeV/c)	E_{D^0} (GeV)			(GeV/c)^2	(GeV/c)	(GeV)	
0–0.3	0–30	$-0.90\pm0.63\pm0.11$	0.50	0.46	0.19	24.3	0.62
0–0.3	30–50	$-0.19\pm0.48\pm0.06$	0.60	0.69	0.20	39.1	0.74
0–0.3	>50	$+0.07\pm0.68\pm0.06$	0.69	1.17	0.20	59.2	0.84
0.3–0.7	0–30	$-0.18\pm0.37\pm0.04$	0.51	0.47	0.51	24.6	0.63
0.3–0.7	30–50	$+0.10\pm0.26\pm0.04$	0.60	0.62	0.51	39.5	0.75
0.3–0.7	>50	$-0.04\pm0.36\pm0.05$	0.69	0.73	0.51	59.0	0.83
0.7–1	0–30	$-0.42\pm0.44\pm0.05$	0.50	0.45	0.85	24.7	0.62
0.7–1	30–50	$-0.36\pm0.29\pm0.04$	0.61	0.60	0.85	39.2	0.75
0.7–1	>50	$+1.49\pm0.42\pm0.15$	0.69	0.76	0.84	58.6	0.83
1–1.5	0–30	$-0.30\pm0.35\pm0.03$	0.54	0.41	1.23	25.3	0.66
1–1.5	30–50	$+0.13\pm0.23\pm0.01$	0.64	0.55	1.24	39.2	0.77
1–1.5	>50	$-0.20\pm0.33\pm0.02$	0.71	0.73	1.24	58.3	0.85
>1.5	0–30	$+0.38\pm0.49\pm0.04$	0.56	0.47	1.84	25.6	0.69
>1.5	30–50	$0.00\pm0.25\pm0.02$	0.65	0.70	1.92	39.9	0.79
>1.5	>50	$+0.36\pm0.33\pm0.04$	0.69	0.60	1.95	59.9	0.86

Table 6: Asymmetries $A^{\gamma N\to D^0X}$ for the $D^*_{K\pi\pi^0}$ sample in bins of ($p_T^{D^0}$, E_{D^0}) together with the weighted (with w_S^2) averages of several kinematic variables. First uncertainty is statistical, second is systematic.

Bin limits		$A^{\gamma N\to D^0X}$	$\langle y\rangle$	$\langle Q^2\rangle$	$\langle p_T^{D^0}\rangle$	$\langle E_{D^0}\rangle$	$\langle D\rangle$
$p_T^{D^0}$ (GeV/c)	E_{D^0} (GeV)			(GeV/c)^2	(GeV/c)	(GeV)	
0–0.3	0–30	$-0.63\pm1.29\pm0.08$	0.52	0.75	0.19	24.4	0.65
0–0.3	30–50	$+0.27\pm1.17\pm0.06$	0.67	0.65	0.20	38.8	0.81
0–0.3	>50	$-2.55\pm2.00\pm0.27$	0.72	1.12	0.19	59.3	0.86
0.3–0.7	0–30	$-0.24\pm0.80\pm0.04$	0.53	0.51	0.52	24.3	0.65
0.3–0.7	30–50	$+0.49\pm0.69\pm0.06$	0.65	0.65	0.51	39.0	0.79
0.3–0.7	>50	$-1.28\pm1.03\pm0.14$	0.72	0.77	0.51	59.1	0.86
0.7–1	0–30	$+0.55\pm0.95\pm0.06$	0.53	0.41	0.84	24.6	0.65
0.7–1	30–50	$-0.53\pm0.76\pm0.06$	0.63	0.53	0.86	39.4	0.77
0.7–1	>50	$-0.17\pm1.00\pm0.03$	0.73	0.80	0.85	58.2	0.88
1–1.5	0–30	$+1.35\pm0.86\pm0.14$	0.54	0.38	1.24	25.4	0.67
1–1.5	30–50	$-0.11\pm0.51\pm0.01$	0.64	0.59	1.25	39.6	0.78
1–1.5	>50	$-0.05\pm0.78\pm0.01$	0.74	0.62	1.25	58.3	0.88
>1.5	0–30	$-0.19\pm1.14\pm0.03$	0.56	0.52	1.80	25.7	0.70
>1.5	30–50	$-0.23\pm0.51\pm0.03$	0.66	0.66	1.88	40.0	0.80
>1.5	>50	$+0.26\pm0.90\pm0.04$	0.74	0.88	1.92	57.3	0.88

5 Determination of the gluon polarisation

In this Section we present the results of our measurement of the gluon polarisation. The extraction of $\Delta g/g$ from $A^{\gamma N}$ at LO QCD accuracy is discussed in Sec. 5.1. The LO determination of the gluon polarisation by a statistically optimised method is described in Sec. 5.2. The extraction of $\Delta g/g$ from $A^{\gamma N}$ at NLO accuracy is presented in Sec. 5.3.

This analysis neglects any contribution from 'intrinsic charm', *i.e.* nonperturbative charm quark or charmed hadron components of the nucleon wave function. Such contributions, estimated to be $\lesssim 1\%$ [34, 35], are fundamentally different from the perturbative splitting of a gluon into a $c\bar{c}$ pair; the latter decreases strongly with x_B. In the EMC measurement of the charm component in the nucleon structure function $F_2^{c\bar{c}}$ [20], a possible intrinsic charm contribution of about 1% at $x_B \sim 0.4$ could not be excluded [20, 21]. Up to now, the estimates of Refs [34, 35] cannot be experimentally verified due to the poor statistics of the EMC measurement at large x_B, too low values of x_B in the HERA $F_2^{c\bar{c}}$ measurements [36], and kinematic acceptance limited to the region $x_B \lesssim 0.1$ for open charm production in COMPASS.

The contribution of resolved-photon interactions was estimated using the RAPGAP generator [37] and found to be negligible in our kinematic domain.

5.1 Leading Order results from the asymmetries

The information on the gluon polarisation contained in $A^{\mu N}$ can be decomposed at LO accuracy as

$$A^{\mu N} = DA^{\gamma N} = a_{LL}\frac{\Delta g}{g}\,, \tag{12}$$

assuming photon-gluon fusion as the underlying partonic process. Here a_{LL} is the analysing power (also called 'partonic asymmetry') of the $\mu g \to \mu' c\bar{c}$ process.

The analysing power a_{LL} depends on partonic kinematics. It is not accessible experimentally on an event-by-event basis. It is obtained using the Monte Carlo generator AROMA [28] in leading order QCD approximation, *i.e.* with parton showers switched off. The generated D^0 events are processed with GEANT [29] to simulate the full response of the COMPASS spectrometer, and then are reconstructed with the same analysis chain as used for real events. In order to provide a_{LL} values for real data, a Neural Network with the same architecture as described in Sec. 4 is used to parameterise the generated a_{LL} in terms of measured kinematic variables X. Here the input layer contains the following observables: $X = \{Q^2, y, x, p_T^{D^0}, E_{D^0}\}$. As a result, $a_{LL}(X)$ is obtained for real data on an event-by-event basis.

Contrary to the parameterisation of $s/(s+b)$, the Neural Network predicts values for a_{LL} based on event kinematics. For each generated event, the network tunes the strength of each variable-neuron and neuron-neuron connection. The strengths are obtained by minimising the squared deviation between the expected output, *i.e.* the generated a_{LL}, and the actual Neural Network prediction for a_{LL} based on X. This training process stops when the deviation between generated and parameterised a_{LL} reaches a stable minimum. Six separate $a_{LL}(X)$ parameterisations were built: for three D meson decay channels ($K\pi$, $K\pi\pi^0$, $K\pi\pi\pi$), each for two experimental configurations (2002–2004 and 2006–2007). The correlation achieved between the generated and the parametrised analysing powers is 77% for the $D^*_{K\pi\pi^0}$ channel and 82% for the remaining channels. The trained network is applied to real data.

Knowing that $A^{\mu N} = DA^{\gamma N}$, the determination of the gluon polarisation from Eq. (12) is straightforward. The extraction of $\Delta g/g$ from $A^{\gamma N}$ in bins of $(p_T^{D^0}, E_{D^0})$ is performed using the values of $\langle a_{LL}/D\rangle$ shown in Table 8.

The gluon polarisation in LO QCD, obtained from $A^{\gamma N}$ amounts to

$$\left\langle \frac{\Delta g}{g} \right\rangle = -0.10 \pm 0.22\ (\text{stat.}) \pm 0.09\ (\text{syst.}) \tag{13}$$

in the range of $0.06 < x < 0.22$ with a weighted $\langle x \rangle \approx 0.11$, and a scale $\langle \mu^2 \rangle \approx 13$ $(\mathrm{GeV}/c)^2$. The range of x is determined by the r.m.s. value of a Gaussian distribution in $\log_{10} x$. Assuming that $\Delta g/g(x)$ is approximately a linear function of x in the range covered by the present data, the above result corresponds to the gluon polarisation $\Delta g/g$ at the value $\langle x \rangle$.

The sources of systematic uncertainties in the measurement of $\Delta g/g$ are listed in Table 9. The contributions from P_μ, P_t, f, $s/(s+b)$ and D are the same as discussed in Sec. 4.2. Contributions from false asymmetries and from the assumption given in Eq. (9), the same as in the statistically optimised method, are discussed in Sec. 5.2. In order to estimate the influence of the simulation parameters on the determination of a_LL, Monte Carlo samples with different parameter sets are generated and the analysing power is recalculated. In these parameter sets, the mass of the charm quark is varied between 1.3 GeV/c^2 and 1.6 GeV/c^2, and the parton distribution functions as well as the factorisation scale is varied by a factor of eight. From each of these systematic tests a new value of $\langle a_\mathrm{LL}/D \rangle$ is obtained, and thereafter $\Delta g/g$ is recalculated for each $(p_\mathrm{T}^{\mathrm{D}^0}, E_{\mathrm{D}^0})$ bin by dividing $A^{\gamma\mathrm{N}}$ by $\langle a_\mathrm{LL}/D \rangle$. The systematic uncertainty in each bin is determined from the average spread of $\Delta g/g$ compared to the result of the default analysis. The value for the systematic uncertainty of gluon polarisation is obtained as a weighted average of the systematic uncertainty in each bin. The relative uncertainty introduced by a_LL alone is 15%.

The final systematic uncertainty of $\langle \Delta g/g \rangle$ is obtained as a quadratic sum of all contributions.

Table 7: Asymmetries $A^{\gamma N\to D^0X}$ for the $D^*_{K\pi\pi\pi}$ sample in bins of ($p_T^{D^0}$, E_{D^0}) together with the weighted (with w_S^2) averages of several kinematic variables. First uncertainty is statistical, second is systematic.

Bin limits		$A^{\gamma N\to D^0X}$	$\langle y\rangle$	$\langle Q^2\rangle$	$\langle p_T^{D^0}\rangle$	$\langle E_{D^0}\rangle$	$\langle D\rangle$
$p_T^{D^0}$ (GeV/c)	E_{D^0} (GeV)			(GeV/c)^2	(GeV/c)	(GeV)	
0–0.3	0–30	$+7.03 \pm 4.74 \pm 0.71$	0.46	0.38	0.22	27.7	0.58
0–0.3	30–50	$-2.05 \pm 1.10 \pm 0.21$	0.60	0.72	0.20	40.6	0.74
0–0.3	> 50	$+0.17 \pm 1.83 \pm 0.05$	0.69	0.88	0.20	59.1	0.84
0.3–0.7	0–30	$-0.59 \pm 1.74 \pm 0.06$	0.52	0.31	0.53	27.8	0.71
0.3–0.7	30–50	$+1.00 \pm 0.54 \pm 0.11$	0.61	0.44	0.52	39.7	0.80
0.3–0.7	> 50	$-1.75 \pm 0.84 \pm 0.18$	0.68	0.70	0.51	60.2	0.84
0.7–1	0–30	$+2.91 \pm 2.61 \pm 0.30$	0.45	0.26	0.84	27.7	0.61
0.7–1	30–50	$+1.42 \pm 0.57 \pm 0.15$	0.64	0.57	0.85	40.9	0.81
0.7–1	> 50	$+1.69 \pm 0.81 \pm 0.17$	0.69	0.58	0.86	60.9	0.84
1–1.5	0–30	$-1.89 \pm 2.64 \pm 0.19$	0.46	0.31	1.22	27.7	0.64
1–1.5	30–50	$-0.45 \pm 0.51 \pm 0.05$	0.63	0.58	1.23	41.1	0.79
1–1.5	> 50	$+1.06 \pm 0.66 \pm 0.11$	0.71	0.77	1.24	61.8	0.86
> 1.5	0–30	$+1.64 \pm 3.52 \pm 0.17$	0.46	0.40	1.84	28.1	0.72
> 1.5	30–50	$+0.44 \pm 0.68 \pm 0.05$	0.65	0.75	1.95	42.2	0.78
> 1.5	> 50	$+0.08 \pm 0.63 \pm 0.02$	0.74	0.77	2.03	64.4	0.88

Table 8: The average LO photon-gluon asymmetries, $\langle a_{\rm LL}/D\rangle$, in bins of ($p_{\rm T}^{\rm D^0}$, $E_{\rm D^0}$) for each $\rm D^0$ decay mode studied in the analysis. The averages use $a_{\rm LL}^{\rm LO}/D$ from data events, obtained from the Neural Network parameterisation; they are weighted with $w_{\rm S}^2$.

Bin limits		**Photon-gluon asymmetries**		
$p_{\rm T}^{\rm D^0}$ (GeV/c)	$E_{\rm D^0}$ (GeV)	$\rm D^0_{K\pi}$, $\rm D^*_{K\pi}$ and $\rm D^*_{K_{sub}\pi}$ samples **c**ombined	$\rm D^*_{K\pi\pi^0}$ sample	$\rm D^*_{K\pi\pi\pi}$ sample
0–0.3	0–30	0.65	0.62	0.64
0–0.3	30–50	0.68	0.65	0.63
0–0.3	>50	0.76	0.74	0.74
0.3–0.7	0–30	0.46	0.42	0.38
0.3–0.7	30–50	0.50	0.46	0.41
0.3–0.7	>50	0.56	0.53	0.52
0.7–1	0–30	0.26	0.19	0.25
0.7–1	30–50	0.26	0.21	0.25
0.7–1	>50	0.29	0.26	0.30
1–1.5	0–30	0.00	-0.06	0.02
1–1.5	30–50	0.01	-0.05	0.04
1–1.5	>50	0.05	-0.02	0.08
>1.5	0–30	-0.23	-0.29	-0.26
>1.5	$30-50$	-0.26	-0.31	-0.23
>1.5	>50	-0.27	-0.31	-0.22

Table 9: Contributions to the systematic uncertainty of $\langle\Delta g/g\rangle^{\rm LO}$ obtained from $A^{\gamma \rm N}$.

Source	$\delta(\langle\Delta g/g\rangle)$	Source	$\delta(\langle\Delta g/g\rangle)$
Beam polarisation P_μ	0.005	$s/(s+b)$	0.007
Target polarisation $P_{\rm t}$	0.005	False asymmetry	0.080
Dilution factor f	0.002	$a_{\rm LL}$	0.015
Assumption, Eq. (9)	0.025	Depolarisation factor D	0.002
Total uncertainty 0.086			

5.2 Statistically optimised determination of the gluon polarisation at LO

The data described in Sec. 3 allow for the determination of $\langle \Delta g/g \rangle$ in a different, statistically optimised way. Practically it means that the gluon polarisation is obtained by replacing the factor D with a_{LL} in the definition of w_{S}: $w_S = P_\mu f a_{\mathrm{LL}} s/(s+b)$. The use of this weight allows us to reproduce the results on $\langle \Delta g/g \rangle$ obtained from $A^{\gamma \mathrm{N}}(\langle p_{\mathrm{T}}^{\mathrm{D}^0} \rangle, \langle E_{\mathrm{D}^0} \rangle)$ with about 6% gain in the statistical precision. This gain is due to a wide range of a_{LL} values but the observed (anti)correlation between the signal purity and the parameterised a_{LL} has to be accounted for in the parameterisation of $s/(s+b)$. This fact is crucial to obtain an unbiased result of $\langle \Delta g/g \rangle$ with this statistically optimised method.

Values for $\langle \Delta g/g \rangle$ and the background asymmetry $\langle A_{\mathrm{B}}^{\gamma \mathrm{N}} \rangle$ were obtained for each of the 48 weeks of data taking and separately for each of the five event samples. The results shown in Table 10 are the weighted means of those values.

Table 10: Results for $\langle \Delta g/g \rangle$ and $\langle A_{\mathrm{B}}^{\gamma \mathrm{N}} \rangle$ for each data sample. Errors are statistical.

	$\mathrm{D}^*_{\mathrm{K}\pi}$	$\mathrm{D}^*_{\mathrm{K}\pi\pi^0}$	$\mathrm{D}^*_{\mathrm{K}\pi\pi\pi}$	$\mathrm{D}^*_{\mathrm{K_{sub}}\pi}$	$\mathrm{D}^0_{\mathrm{K}\pi}$
$\langle \Delta g/g \rangle$	-0.192 ± 0.305	-0.414 ± 0.575	0.614 ± 0.667	0.497 ± 0.995	0.020 ± 0.415
$\langle A_{\mathrm{B}}^{\gamma \mathrm{N}} \rangle$	$+0.019 \pm 0.029$	$+0.051 \pm 0.035$	$+0.004 \pm 0.036$	$+0.004 \pm 0.047$	-0.005 ± 0.004

The value of the gluon polarisation is obtained as the weighted mean of the five results shown in Table 10 and amounts to

$$\left\langle \frac{\Delta g}{g} \right\rangle = -0.06 \pm 0.21\ (\text{stat.}) \pm 0.08\ (\text{syst.}) \tag{14}$$

in the range of $0.06 < x < 0.22$ with a weighted $\langle x \rangle \approx 0.11$, and a scale $\langle \mu^2 \rangle \approx 13\ (\mathrm{GeV}/c)^2$.

The major contributions for the systematic uncertainty given in Eq. (14) are presented in Table 11. They were estimated as follows. In addition to P_μ, P_{t}, f and $s/(s+b)$, the uncertainty of a_{LL} was also determined from the spread of weights $\langle w w_0 \rangle / \langle w_0^2 \rangle$ (where w_0 stands for the default analysis). The use of different sets of parameters as described in Sec. 5.1 gives rise to a relative systematic uncertainty of 9% of the $\langle \Delta g/g \rangle$ value originating from a_{LL}. The relative systematic uncertainty introduced by $s/(s+b)$ is 7%.

In order to study the influence of false asymmetries, the $\mathrm{D}^*_{\mathrm{K}\pi}$ sample was divided into two sub-samples using criteria related to the experimental apparatus, *e.g.* the slow pion going to the left or to the right side of the incoming muon. The resulting asymmetries were found to be compatible within their statistical accuracies, *i.e.* no false asymmetries were observed. An upper limit of the contribution of time dependent acceptance effects to the systematic uncertainty was derived from the dispersion of $\langle \Delta g/g \rangle$ and $\langle A_{\mathrm{B}}^{\gamma \mathrm{N}} \rangle$ in the 48 weeks of data taking. The study was performed using the background asymmetry, profiting from the large statistics. Then the obtained results were translated to $\langle \Delta g/g \rangle$ using the method described in Ref. [27]. An uncertainty of 0.024 was obtained assuming that possible detector instabilities are similar for background and signal events. Notice that the same assumption was used to reduce the number of unknowns in Eq. (5) from 12 to 9. Therefore, a more conservative approach is taken: the double ratio of acceptances for the signal, $\alpha_{\mathrm{S}}^u \cdot \alpha_{\mathrm{S}}^{d'} / \alpha_{\mathrm{S}}^d \cdot \alpha_{\mathrm{S}}^{u'}$, is assumed to be uncorrelated with the corresponding one for the background events. The combination of these two cases leads to an upper limit of 0.08 for the possible contribution of false asymmetries. This contribution is also used in Sections 4.2 and 5.1.

An uncertainty originating from the assumption for $\Delta g/g$, analogous to that given in Eq. (9) and valid for $\Delta g/g$ constant in the measured interval, $0.06 < x < 0.22$, is estimated as follows. First a pair of extremal values of $\Delta g/g$ in that interval is selected as those given by the COMPASS NLO QCD fit with $\Delta g > 0$, see Sec. 5.3. This fit is chosen to maximise a potential influence of the above assumption. Next, a

Table 11: Contributions to the systematic uncertainty of $\langle \Delta g/g \rangle^{\mathrm{LO}}$ obtained in a statistically optimised method.

Source	$\delta(\langle \Delta g/g \rangle)$	Source	$\delta(\langle \Delta g/g \rangle)$
Beam polarisation P_μ	0.003	$s/(s+b)$	0.004
Target polarisation P_t	0.003	a_{LL}	0.005
Dilution factor f	0.001	False asymmetry	0.080
Assumption, Eq. (9)	0.025		
Total uncertainty	0.084		

difference between these two $\Delta g/g$ values is used as a bias in the system of equations from which $\Delta g/g$ and $A_{\mathrm{B}}^{\gamma \mathrm{N}}$ are determined. The bias is added to all $\langle \Delta g/g \rangle_{w_{\mathrm{B}}\beta_{\mathrm{S}}}$ terms while the $\langle \Delta g/g \rangle_{w_{\mathrm{S}}\beta_{\mathrm{S}}}$ ones are left unchanged. The $\Delta g/g$ interval resulting from the equations gives a relative systematic uncertainty due to the assumption. Possible variations of $A_{\mathrm{B}}^{\gamma \mathrm{N}}$ are studied in a similar way using a parameterisation of the inclusive asymmetry, A_1^{d}, [38]. The systematic uncertainty on $\Delta g/g$ is taken as the largest difference between the result obtained in the default analysis and results of those tests.

The result given in Eq. (14) is shown in Fig. 10 together with a compilation of other LO gluon polarisation measurements from high-p_{T} hadron production by COMPASS [15, 18], SMC [13] and HERMES [14]. The present measurement is at a scale of about 13 (GeV/c)^2 while other measurements are at 3 (GeV/c)^2.

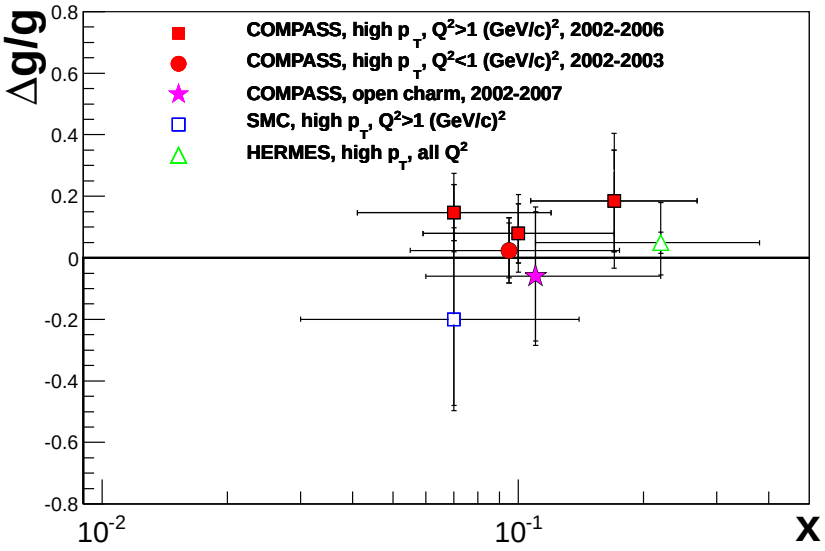

Figure 10: A compilation of gluon polarisation measurements from open charm and high-p_{T} hadron production. The star denotes a result of the present, open charm analysis, Eq. (14), obtained at LO accuracy, 2002–2007 data and all values of Q^2. Full squares denote a COMPASS result [18] for high-p_{T} hadron production on 2002–2006 data, for $Q^2 > 1$ (GeV/c)^2 while a full circle corresponds to 2002–2003 data and $Q^2 < 1$ (GeV/c)^2 [15]. The empty square shows the SMC measurement [13] for $Q^2 > 1$ (GeV/c)^2 and the empty triangle the HERMES result [14] obtained for all values of Q^2. The horizontal bars mark the range in x for each measurement, the vertical ones give the statistical precision or the total uncertainties.

5.3 Next to Leading Order results

The extraction of the gluon polarisation as described in Secs 5.1 - 5.2 was performed at LO where the only process leading to open-charm production is PGF. This requires knowledge of the analysing power a_{LL} and the signal strength on a bin-by-bin or event-by-event basis. Only combinatorial background was considered in the LO analysis.

In this section a brief outline of a method of computing the NLO QCD corrections to the a_{LL} calculation in our analysis is given, see also Ref. [39]. Examples of the NLO processes contributing to the muoproduction of the $c\bar{c}$ pair are shown in Fig.11. Apart from the NLO corrections to the PGF mechanism, Fig.11 a-c, there exists yet other NLO contributions to muoproduction of open-charm, initiated by light quarks; as an example a process where a gluon emitted by a light quark creates the $c\bar{c}$ pair is shown in Fig. 11d. Such processes do not probe the gluons inside the nucleon albeit they contribute to the D meson signal. Therefore, in the extraction of the gluon polarisation at NLO accuracy from the signal asymmetries, a correction term has to be taken into account:

$$A^{\gamma \mathrm{N}} = \frac{a_{\mathrm{LL}}}{D}\frac{\Delta g}{g} + A_{\mathrm{corr}}.$$

Here, a_{LL} is calculated at NLO accuracy and is different from the corresponding one at LO.

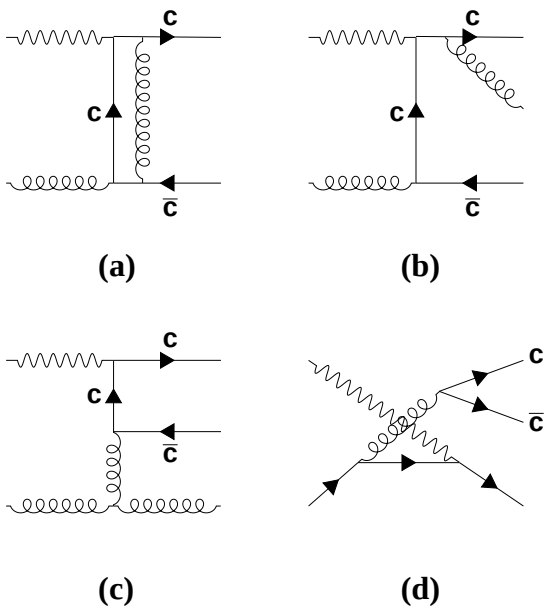

Figure 11: Examples of the NLO processes contributing to the muoproduction of the $c\bar{c}$ pair: a) virtual correction, b), c) gluon bremsstrahlung, d) light quark background

The QCD calculations at NLO accuracy for spin averaged [40] as well as polarisation dependent cross sections for open charm production [41] are available only at the photoproduction limit, *i.e.* for $Q^2 = 0$. They are used in our analysis to estimate the value of the NLO corrections to a_{LL} and the light quark contribution. The average value of Q^2 in the kinematic region of our measurement is about 0.6 $(\mathrm{GeV}/c)^2$. It was confirmed by a direct check at LO accuracy that the $Q^2 = 0$ limit used in the calculation is a very good approximation in our kinematic domain.

Note that only one D meson is registered in the COMPASS data, while the second charm particle is unobserved. Also the NLO calculations of Refs [40, 41] represent integrated cross sections for a single charm quark (meson) observed in the final state. The cross sections are integrated over the kinematic

variables of the 'unobserved' second charm quark and radiated hard gluon, present in NLO processes. The limits of the integration depend on the available phase-space, left for 'unobserved' partons which is determined by x and the kinematics of the D-tagged c quark.

In order to obtain $a_{\rm LL}$ in NLO accuracy on an event-by-event basis, the AROMA generator (which is based on a LO matrix element) with parton showers included is used, followed by a full simulation of the detector. In this way an approximation to the phase space needed for NLO QCD corrections is provided.

For every simulated event, the upper limit of the integration over the energy of the unobserved gluon in the NLO emission process, $\gamma^* g \to c\bar{c}g$, is obtained from the partonic Mandelstam variables, $\hat{s}$ and $\hat{t}$. Both variables are calculated from the kinematics of simulated events. In particular $\hat{s}$ is determined from x, $x_{\rm B}$ and Q^2 while $\hat{t}$ is related to the kinematics of the D-tagged charm quark. The integration over unobserved NLO real gluon emission reduces a differential cross section for a three-body final state ($c\bar{c}g$) to that for a two-body one ($c\bar{c}$), which has to be added to the LO cross section ($c\bar{c}$, PGF) and the two-body virtual corrections (see *e.g.* diagram (a) in Fig. 11). In this way a correct infra-red divergence cancellation is achieved [41]. The semi-inclusive partonic cross section at NLO accuracy is calculated on an event-by-event basis for both spin averaged and spin dependent case using formulae of Ref. [41], and consequently $a_{\rm LL}$ at NLO accuracy is obtained. The same procedure is applied for the correction originating from a light quark. It should be stressed that in this method of $a_{\rm LL}$ estimation at NLO, only the values of $\hat{s}$ and $\hat{t}$ are taken from AROMA simulated events.

To obtain the gluon polarisation at NLO accuracy, the measured asymmetry for D meson production has to be combined with the $a_{\rm LL}$ calculated at NLO. The kinematic variables $p_{\rm T}^{\rm D^0}$, $E_{\rm D^0}$ and gluon momentum fraction x define the total energy of all particles produced in the final state of the partonic process, including unobserved gluons emitted at NLO accuracy, $\gamma^* g \to c\bar{c}g$. However, in $a_{\rm LL}$ calculations, simulated events at given x values are used and the integration over energy of the unobserved gluon is performed to obtain divergence-free $a_{\rm LL}$, which depends on $\hat{s}$ and $\hat{t}$ only. Therefore to be consistent with the NLO method of calculating $a_{\rm LL}$, the asymmetry measured in ($p_{\rm T}^{\rm D^0}$, $E_{\rm D^0}$) intervals is binned into five one-dimensional intervals of $p_{\rm T}^{\rm D^0}$ only.

Table 12: The average values of the $\langle a_{\rm LL}/D \rangle$ and $A_{\rm corr}$, at NLO and in bins of $p_{\rm T}^{\rm D^0}$ for each $\rm D^0$ decay mode studied in the analysis.

$p_{\rm T}^{\rm D^0}$ (GeV/c)	$\rm D^0_{K\pi}$, $\rm D^*_{K\pi}$ and $\rm D^*_{K_{sub}\pi}$ samples combined		$\rm D^*_{K\pi\pi^0}$ sample		$\rm D^*_{K\pi\pi\pi}$ sample	
	$\langle a_{\rm LL}/D \rangle$	$A_{\rm corr}$	$\langle a_{\rm LL}/D \rangle$	$A_{\rm corr}$	$\langle a_{\rm LL}/D \rangle$	$A_{\rm corr}$
0.0–0.3	−0.130	0.001	−0.127	0.002	−0.097	0.000
0.3–0.7	−0.241	0.003	−0.263	0.003	−0.240	0.001
0.7–1.0	−0.419	0.005	−0.460	0.004	−0.404	0.002
1.0–1.5	−0.574	0.008	−0.607	0.008	−0.572	0.006
> 1.5	−0.679	0.027	−0.710	0.020	−0.719	0.021

In each $p_{\rm T}^{\rm D^0}$ bin, the weighted averages of $a_{\rm LL}/D$ and $A_{\rm corr}$ are calculated, Table 12, and the gluon polarisation is evaluated from the $A^{\gamma \rm N \to D^0 X}$ asymmetries. The NLO light quark contribution to the D meson asymmetry, $A_{\rm corr}$, is small, less than 5%, compared to the measured asymmetries. The gluon

polarisation at NLO accuracy, obtained as weighted average over all $p_{\mathrm{T}}^{\mathrm{D}^0}$ bins, is:

$$\left\langle \frac{\Delta g}{g} \right\rangle^{\mathrm{NLO}} = -0.13 \ \pm \ 0.15 \ \ (\mathrm{stat.}) \pm 0.15 \ \ (\mathrm{syst.}) \tag{15}$$

It is determined in the interval $0.12 \ < x < 0.33$ with a weighted $\langle x \rangle \approx 0.20$, at the scale $\langle \mu^2 \rangle \approx 13$ $(\mathrm{GeV}/c)^2$. The gluon momentum fraction x is taken from the simulations.

For a given experimental acceptance for open charm tagging, the average value of x depends on the order of the QCD calculations used in the analysis. At the same time the energy in the photon-gluon centre-of-mass system required to produce a D^0 meson is higher with parton shower simulation as compared to the case of LO where parton shower is not simulated. Therefore a value of $\langle x \rangle$ at which the gluon polarisation is determined at NLO $\langle x \rangle^{\mathrm{NLO}} \approx 0.20$, is higher than $\langle x \rangle^{\mathrm{LO}} \approx 0.11$, see for example Fig. 12.

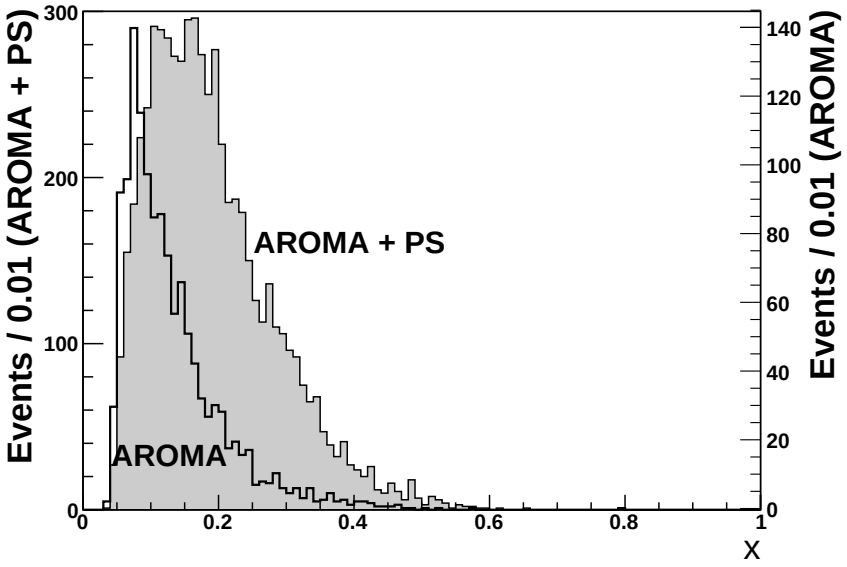

Figure 12: Distributions of the gluon momentum fractions x for the simulated $\mathrm{D}^*_{\mathrm{K}\pi}$ events at the LO accuracy (marked 'AROMA') and at LO with parton shower (AROMA + PS). Note different normalisations of the samples.

A systematic uncertainty of the result in Eq. (15) is estimated as follows, see Table 13. Contributions from P_μ, P_{t}, f, $s/(s+b)$ and D are the same as discussed in Sec. 4.2, *i.e.* 5%, 5%, 2%, 7% and 1.6% respectively. Contributions from false asymmetries and the assumption given in Eq. (9), the same as in the statistically optimised method at LO, are discussed in Sec.5.2. Concerning the partonic asymmetry a_{LL}, the following contributions resulting from the NLO determination of a_{LL} were studied: its dependence on scale, the charm mass value and the Monte Carlo mode (with or without PS). The renormalisation scale (here chosen equal to the factorisation one, Ref. [41]) varied from m_{c} to $3m_{\mathrm{c}}$. This changes the gluon polarisation at most by a factor of two, leading to a conservative contribution to the systematic uncertainty of 0.1. The variation of the charm quark mass between 1.3 and 1.6 GeV/c^2 results in a contribution of 0.05. The systematic uncertainty contribution from the simulation method was estimated using AROMA with and without parton showers. Note, that measured D meson spectra are described reasonably well by AROMA both with and without parton showers, and the difference in a_{LL} between both cases is mainly due to the different phase space available for 'unobserved' partons. Such comparison allows us to give a conservative estimate of uncertainty due to the simulation method equal to 0.04. The total systematic uncertainty of $\langle \Delta g/g \rangle^{\mathrm{NLO}}$ is obtained by adding all the contributions in quadrature and amounts to 0.15.

Table 13: Contributions to the systematic uncertainty of $\langle \Delta g/g \rangle^{\mathrm{NLO}}$.

Source	$\delta(\langle \Delta g/g \rangle)$	Source	$\delta(\langle \Delta g/g \rangle)$
Beam polarisation P_μ	0.006	$s/(s+b)$	0.009
Target polarisation P_t	0.006	a_{LL}	0.119
Dilution factor f	0.003	False asymmetry	0.080
Assumption, Eq. (9)	0.025	Depolarisation factor D	0.002
Total uncertainty 0.146			

The result on $\langle \Delta g/g \rangle^{\mathrm{NLO}}$, Eq. (15), was included in NLO QCD fits of polarised parton distributions, see Appendix for details. The fitted distributions of $\Delta g(x)/g(x)$, evolved to $Q^2 = 13$ (GeV/c)^2, are shown in Fig. 13 together with error bands corresponding to the statistical errors as derived from the error matrix of the fitted parameters. The present NLO open charm result agrees within 0.5 standard deviation with the fitted COMPASS curve for $\Delta g(x) < 0$ and within 2 σ with the one for $\Delta g(x) > 0$. It significantly influences the $\Delta g(x) > 0$ fit, reducing the value of ΔG from 0.39 ± 0.07 (stat.) to 0.22 ± 0.08 (stat.) at Q^2 = 3 (GeV/c)^2.

The results of two other global fits, DSSV [42] and LSS [12], which employ both DIS and SIDIS asymmetries are also shown in the same Figure. In the DSSV fit, $\Delta g(x)$ changes sign at $x \approx 0.1$ and is about 1.5 σ above the COMPASS open charm value. In the case of LSS, two solutions, with positive and with sign-changing $\Delta g(x)$ are quoted. The LSS fit cannot distinguish between the positive and sign-changing $\Delta g(x)$ functions. Both solutions give a positive $\Delta g(x)$ at the (x, Q^2) of the present measurement, about 2 and 1.3 σ above the measured value.

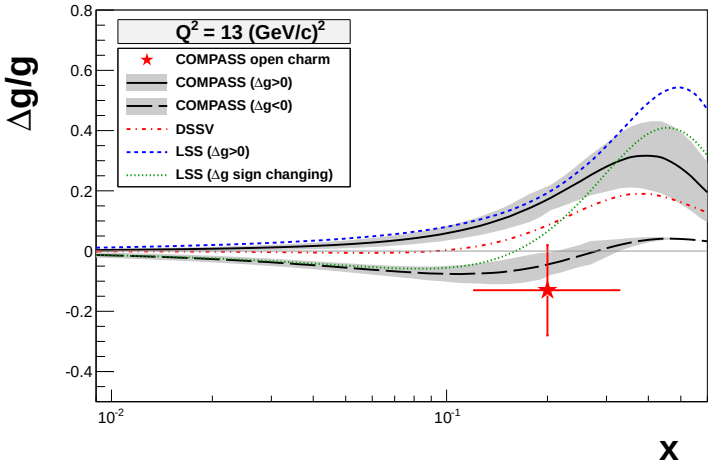

Figure 13: The present NLO measurement of the gluon polarisation $\langle \Delta g(x)/g(x) \rangle$ at $\langle \mu^2 \rangle = 13$ (GeV/c)^2, compared to the NLO QCD fits of COMPASS with $\Delta g(x) > 0$ (continuous line) and $\Delta g(x) < 0$ (long-dashed) with their respective error bands, of LSS [12] (dashed and dotted curves, respectively with $\Delta g > 0$ and Δg changing sign) and of DSSV [42] (dashed-dotted curve), all at the same value of Q^2 = 13 (GeV/c)^2. The measurement error and the error bands are statistical only; the horizontal bar marks the range of x in which $\langle \Delta g(x)/g(x) \rangle$ is determined.

6 Conclusions

We have presented new results on the gluon polarisation in the nucleon $\langle \Delta g/g \rangle$ and the virtual photon-nucleon asymmetries $A^{\gamma \mathrm{N}}$ obtained from charm production tagged by D meson decays in 160 GeV/c polarised muon scattering off polarised proton and deuteron targets. The results are based on a data

sample collected between 2002 and 2007 and supersede the previously published ones [19] as they are based on an enlarged data sample and an improved analysis method. The gluon polarisation is determined with open charm production dominated by the photon-gluon fusion mechanism followed by a spin-independent charm quark fragmentation into D mesons. This analysis neglects any contributions from the intrinsic charm; a contribution of resolved photon interactions was found negligible.

Only one charmed meson is required in every event. This meson is selected through its decay in one of the following channels: $D^*(2010)^+ \to D^0\pi^+_{\rm slow} \to (K\pi/K\pi\pi^0/K\pi\pi\pi)\pi^+_{\rm slow}$ or $D^0 \to K\pi$. The decays are selected using the invariant mass distributions of identified kaons and pions. A neural network is used to distinguish signal from background events in the data. The asymmetries $A^{\gamma N}$ are extracted from these open charm events in bins of D^0 transverse momentum and laboratory energy. The average gluon polarisation obtained from these asymmetries at LO QCD accuracy amounts to $\langle \Delta g/g \rangle^{\rm LO} = -0.10 \pm 0.22\,(\text{stat.}) \pm 0.09\,(\text{syst.})$. This result is confirmed and statistically improved by employing a statistically optimised method of extracting the gluon polarisation:

$$\left\langle \frac{\Delta g}{g} \right\rangle^{\rm LO} = -0.06 \pm 0.21\,(\text{stat.}) \pm 0.08\,(\text{syst.}).$$

Both results are obtained in the range $0.06 < x < 0.22$ of the gluon momentum fraction with $\langle x \rangle \approx 0.11$ and a scale $\langle \mu^2 \rangle \approx 13\ (\text{GeV}/c)^2$.

For the first time in this analysis, next-to-leading order QCD calculations for the determination of the gluon polarisation are employed. sing asymmetries $A^{\gamma N}$ the gluon polarisation is obtained as:

$$\left\langle \frac{\Delta g}{g} \right\rangle^{\rm NLO} = -0.13 \pm 0.15\,(\text{stat.}) \pm 0.15\,(\text{syst.}).$$

In this case the range of x, $0.12 < x < 0.33$, leads to a higher average value, $\langle x \rangle \approx 0.20$, while the scale is approximately the same, $\langle \mu^2 \rangle \approx 13\ (\text{GeV}/c)^2$.

The present measurement at LO QCD accuracy of the gluon polarisation in the nucleon, together with other measurements of SMC, COMPASS and HERMES, all situated around $x \sim 0.1$, points towards a small gluon polarisation at that value of x. This is a hint for a small value of the first moment, ΔG, of the gluon helicity distribution, although it in principle does not exclude a large value of ΔG.

The $\langle \Delta g/g \rangle^{\rm NLO}$ result was included in NLO QCD fits of polarised parton distributions. It significantly influences a fit in which $\Delta g(x) > 0$ was assumed, reducing the value of ΔG from 0.39 ± 0.07 (stat.) to 0.24 ± 0.09 (stat.) at $Q^2 = 3\ (\text{GeV}/c)^2$, after it is included.

Appendix

In this appendix, new NLO QCD fits of polarised parton distributions, including the $\langle \Delta g/g \rangle^{\rm NLO}$ result of Eq. (15) are presented. In our previous fit [3] the gluon helicity distribution is parametrised at a reference Q^2 of 3 $(\text{GeV}/c)^2$ in the form

$$\Delta g(x) = \frac{\eta_{\rm g}\, x^{\alpha_{\rm g}}\,(1-x)^{\beta_{\rm g}}}{\displaystyle\int_0^1 x^{\alpha_{\rm g}}\,(1-x)^{\beta_{\rm g}}\,{\rm d}x}. \tag{16}$$

Here $\eta_{\rm g}$ is the integral of $\Delta g(x)$, $\eta_{\rm g} \equiv \Delta G$. The same parameterisations, Eq. (16), are used for the singlet, non–singlet quark and gluon helicity distributions except for the singlet quark in the fit with $\eta_g > 0$ where a factor $(1+\gamma x)$ is added in order to allow a change of sign. The high x parameter of the gluon helicity distribution is fixed to $\beta_g = 10$ in this $\eta_g > 0$ fit so that the total number of free parameters remained equal to 10. Two fits, in NLO QCD approximation and using all inclusive data with $Q^2 > 1\ (\text{GeV}/c)^2$ are performed: one with $\eta_{\rm g} > 0$, the other with $\eta_{\rm g} < 0$. Both of them gave a comparable χ^2 probability.

In the new fit all the data used in Ref. [3] are employed with an addition of the 15 COMPASS values of A_1^p published later [43]. As in the previous fit only statistical errors are considered. The reference Q^2 is kept at 3 (GeV/c)^2 and the same parameterisations, Eq. (16), are used. The total number of free parameters is also equal to 10.

The new open charm result is not attached to a precise value of x and thus its contribution is taken into account by the average

$$\langle R_{\rm g}\rangle = \frac{1}{(0.33-0.12)}\int_{0.12}^{0.33}\left[\frac{\Delta g}{g}(x,Q^2=13)\right]{\rm d}x \qquad (17)$$

which is re–evaluated during the fit for any modification of one of the gluon or singlet quark parameters. The obtained value of $\langle R_{\rm g}\rangle$ is compared to the open charm result $v_{\rm OC} = -0.13$ with the statistical error $\sigma_{\rm OC} = 0.15$ and the χ^2 of the fit is incremented by $(\langle R_{\rm g}\rangle - v_{\rm OC})^2/\sigma^2_{\rm OC}$.

The unpolarised gluon distribution $g(x,Q^2)$ in Eq. (17) is taken from the MRST04 parameterisation [44]. It was also used in Ref. [3]. In contrast to previous parameterisations of the same group, MRST04 predicts a slower decrease of the gluon distribution at high x, $(1-x)^\beta$ with $\beta \sim$ 3–4. For this reason the choice of $\beta_{\rm g} = 10$ for the fit with $\eta_{\rm g} > 0$ in Ref. [3] leads to a strongly peaked distribution of $\Delta g/g$ which in turn generates a dip in the fitted distribution of $g_1^{\rm d}(x)$ around $x = 0.25$ for low values of Q^2 and leads in some cases to very asymmetric errors due to the limits imposed by the positivity condition $|\Delta g(x)| \leq g(x)$. To avoid these unphysical features, $\beta_{\rm g}$ is now fixed to 6 in the fit with $\eta_{\rm g} > 0$.

The present open charm result has practically no effect on the fit for $\Delta g(x) < 0$, where $\eta_{\rm g} = -0.34 \pm 0.12$ with- and without that measurement, while it reduces significantly the positive $\eta_{\rm g}$, from $\eta_{\rm g} = 0.39 \pm 0.07$ (stat.) to $\eta_{\rm g} = 0.22 \pm 0.08$ (stat.) at Q^2 = 3 (GeV/c)^2, after it is included. Similarly the values of $\alpha_{\rm g}$ for the fits including the open charm point are $\alpha_{\rm g} = 1.31 \pm 0.47$ (stat.) for $\Delta g(x) > 0$ and $\alpha_{\rm g} = 0.26 \pm 0.48$ (stat.) for $\Delta g(x) < 0$, both at Q^2 = 3 (GeV/c)^2.

Acknowledgments

We gratefully acknowledge discussions with W. Vogelsang on the NLO analysis of our data. We would like to thank the CERN management and staff for their support, as well as the skills and efforts of the technicians of the collaborating institutes.

References

[1] EMC Collaboration, J. Ashman *et al.*, Nucl. Phys. B **328** (1989) 1; Phys. Lett. B **206** (1988) 364.

[2] SMC Collaboration, B. Adeva *et al.*, Phys. Rev. D **58** (1998) 112001.

[3] COMPASS Collaboration, V.Yu. Alexakhin *et al.*, Phys. Lett. B **647** (2007) 8.

[4] E155 Collaboration, P.L. Anthony *et al.*, Phys. Lett. B **463** (1999) 339;
see also references in [3].

[5] HERMES Collaboration, A. Airapetian *et al.*, Phys. Rev. D **75** (2007) 012007;
erratum, ibid. D**76** (2007) 039901.

[6] CLAS Collaboration, K.V. Dharmawardane *et al.*, Phys. Lett. B **641** (2006) 11.

[7] PHENIX Collaboration, A. Adare *et al.*, Phys. Rev. Lett. **103** (2009) 012003.

[8] STAR Collaboration, B.I. Abelev *et al.*, Phys. Rev. Lett. **100** (2008) 232003.

[9] J. Ellis and R. Jaffe, Phys. Rev. D **9** (1974) 1444; *ibid.* **10** (1974) 1669.

[10] S. Bass, *The Spin Structure of the Proton*, World Scientific Publishing (2007).

[11] E. Leader, Phys. Rev. D **83** (2011) 096012.

[12] LSS, E. Leader, A.V. Sidorov and D.B. Stamenov, Phys. Rev. D **82** (2010) 114018.

[13] SMC Collaboration, B. Adeva *et al.*, Phys. Rev. D **70** (2004) 012002.

[14] HERMES Collaboration, A. Airapetian *et al.*, JHEP 1008 (2010) 130.

[15] COMPASS Collaboration, E.S. Ageev *et al.* Phys. Lett. B **633** (2006) 25.

[16] T. Sjöstrand, S. Mrenna and P. Skands, JHEP **0605** (2006) 026;
see also `http://projects.hepforge.org/pythia6/` for recent updates.

[17] G. Ingelman, A. Edin and J. Rathsman, Comput. Phys. Commun. **101** (1997) 108.

[18] COMPASS Collaboration, M.G. Alekseev *et al.*, CERN-PH-EP/2012-010 and to appear in Phys. Lett. B (2012).

[19] COMPASS Collaboration, M.G. Alekseev *et al.*, Phys. Lett. B **676** (2009) 31.

[20] EMC Collaboration, J.J. Aubert *et al.*, Nucl. Phys. B **213** (1983) 31.

[21] B. W. Harris, J. Smith and R. Vogt, Nucl. Phys. B **461** (1996) 181.

[22] COMPASS Collaboration, "D^* and D^0 production in muon nucleon interactions at 160 GeV/c", M.G. Alekseev *et al.*, in preparation.

[23] COMPASS Collaboration, P. Abbon *et al.*, Nucl. Instrum. Meth. A **577** (2007) 455.

[24] N. Doble, L. Gatignon, G. von Holtey and F. Novoskoltsev, Nucl. Instrum. Meth. A **343** (1994) 351.

[25] A.A. Akhundov, D.Yu. Bardin, L. Kalinovskaya and T. Riemann, Fortschr. Phys. **44** (1996) 373.

[26] P. Abbon *et al.*, Nucl. Instrum. Meth. A, **631** (2011) 26.

[27] C. Franco, PhD thesis, Technical University of Lisbon, 2011,
`http://wwwcompass.cern.ch/compass/publications/welcome.html#theses`.

[28] G. Ingelman, J. Rathsman and G.A. Schuler, Comput. Phys. Commun. **101** (1997) 135;
see `http://www.isv.uu.se/thep/aroma/` for recent updates.

[29] See *e.g.* GEANT4 Collaboration, S. Agostinelli *et al.*,. Instrum. Meth. A, **506** (2003) 250;
J. Allison *et al.*, IEEE Trans. on Nucl. Sci. **53** (2006) 270.

[30] J. Pretz and J.M. Le Goff, Nucl. Instrum. Meth. A **602** (2009) 594.

[31] J. Pretz, Nucl. Instrum. Meth. A **659** (2011) 456.

[32] R. Sulej, K. Zaremba, K. Kurek and E. Rondio, i Measur. Sci. Tech. **18** (2007) 2486.

[33] F. Robinet, PhD thesis, University Paris Diderot (Paris 7), 2008,
`http://wwwcompass.cern.ch/compass/publications/welcome.html#theses`.

[34] S.J. Brodsky, C. Peterson and N. Sakai, Phys. Rev. D **23** (1981) 2745.

[35] J. Alwall, extended version of the talk given at the XIIIth Int. Workshop on Deep Inelastic Scattering, Madison, USA, 2005, arXiv:hep-ph/0508126;
J. Alwall and G. Ingelman, Phys. Rev. D **71** (2005) 094015.

[36] ZEUS Collaboration, S. Chekanov *et al.*, Eur. Phys. J. C **65** (2010) 65;
H1 Collaboration, F.D. Aaron *et al.*, Phys. Lett. B **686** (2010) 91.

[37] H. Jung, Comput. Phys. Commun. **86** (1995) 147.

[38] COMPASS Collaboration, V.Yu. Alexakhin *et al.*, Phys. Lett. B **647** (2007) 330.

[39] COMPASS Collaboration, K. Kurek, J. Phys. Conf. Ser. **295** (2011) 012065;
K. Kurek, habilitation thesis, National Centre for Nuclear Reseach, Otwock–Świerk, Poland (2011), `http://wwwcompass.cern.ch/compass/publications/welcome.html#theses`.

[40] W. Beenakker, H. Kuijf, W.L. Neerven and J. Smith, Phys. Rev. D **40** (1989) 54;
J. Smith and W.L. Neerven Nucl. Phys. B **374** (1992) 36.

[41] I. Bojak and M. Stratmann Phys. Lett. B **433** (1998) 411; Nucl. Phys. B **540** (1999) 345;
I. Bojak, PhD thesis, University of Dortmund, 2000, arXiv:hep-ph/0005120v1.

[42] DSSV, D. de Florian, R. Sassot, M. Stratmann and W. Vogelsang, Phys. Rev. D **80** (2009) 034030.

[43] COMPASS Collaboration, M.G. Alekseev *et al.*, Phys. Lett. B **690** (2010) 466.

[44] MRST04, A.D. Martin, R.G. Roberts, W.J. Stirling and R.S. Thorne, Phys. Lett. B **604** (2004) 61.